

A nonhydrostatic version of FVCOM:

1. Validation experiments

Zhigang Lai,¹ Changsheng Chen,^{1,2} Geoffrey W. Cowles,¹ and Robert C. Beardsley³

Received 20 May 2009; revised 15 July 2010; accepted 29 July 2010; published 13 November 2010.

[1] The unstructured grid finite volume coastal ocean model (FVCOM) system has been expanded to include nonhydrostatic dynamics. This addition uses the fractional step method with both split mode explicit and semi-implicit schemes. The unstructured grid finite volume method, combined with a correction of the final free surface from its intermediate value with inclusion of nonhydrostatic effects, efficiently reduces numerical damping and thus ensures second-order accuracy of the solutions with local/global volume conservation. Numerical experiments have been made to fully validate the nonhydrostatic FVCOM, including surface standing and solitary waves in idealized flat- and sloping-bottomed channels in homogeneous conditions, the density adjustment problem for lock exchange flow in a flat-bottomed channel, and two-layer internal solitary wave breaking on a sloping shelf. The model results agree well with the relevant analytical solutions and laboratory data. These validation experiments demonstrate that the nonhydrostatic FVCOM is capable of resolving complex nonhydrostatic dynamics in coastal and estuarine regions.

Citation: Lai, Z., C. Chen, G. W. Cowles, and R. C. Beardsley (2010), A nonhydrostatic version of FVCOM: 1. Validation experiments, *J. Geophys. Res.*, 115, C11010, doi:10.1029/2009JC005525.

1. Introduction

[2] The unstructured grid finite volume coastal ocean model (FVCOM) is a state-of-the-art open source community model that has been applied to global/basin/regional scale ocean, coastal, and estuarine studies [Chen *et al.*, 2003, 2006a, 2006b, 2007]. FVCOM was developed originally with the hydrostatic approximation in which the rate of change, advection, and diffusion of the vertical velocity are ignored and the pressure gradient in the vertical is balanced by gravity. According to scaling analysis, the hydrostatic balance is valid for large-scale motions in regional scale and larger-scale ocean waters, where the horizontal motion is dominant [Mahadevan *et al.*, 1996a; Marshall *et al.*, 1997a]. In coastal and estuarine waters, particularly over shallow banks and the shelfbreak where internal waves can be energetic, and in inlets or narrow river passages, where the motion's horizontal scale can be comparable to the local depth, the flow is influenced by nonhydrostatic dynamics. In these regions, the nonhydrostatic process contributes directly to the generation of high-frequency external/internal waves [Beji and Battjes, 1994; Gerkema, 2001; Vlasenko and

Hutter, 2002; Scotti *et al.*, 2007] and strong vertical stirring during convection [Jones and Marshall, 1993].

[3] Recently, we have implemented nonhydrostatic dynamics into FVCOM. This work was motivated to take advantage of the flexibility of the unstructured grid in refining the grid locally to resolve nonhydrostatic processes with minimum sacrifice of computational efficiency. Because of the requirements of inverting a large sparse matrix for pressure and high horizontal resolution to resolve small-scale flows at a length scale of $O(1-100\text{ m})$, running a nonhydrostatic model over a basin or regional domain needs significant computing powers, which is usually impractical or even intractable. The fact that most nonhydrostatic processes observed in coastal areas are small-scale, localized features makes it more suitable to use an unstructured grid model to locally employ high-resolution grids (where required to resolve the nonhydrostatic dynamics) while maintaining a coarser mesh in the remaining portion of the domain. This approach would enable resolution of complex multiscale dynamical processes and their interactions in an integrated coastal-estuarine system.

[4] To modify the underlying equation system from hydrostatic to nonhydrostatic, the fundamental problem is to find the total pressure (P) with affordable computational costs. Following the traditional approach used in nonhydrostatic ocean models, we decomposed the total pressure into hydrostatic and nonhydrostatic components [see, e.g., Mahadevan *et al.*, 1996b; Marshall *et al.*, 1997b]. Then a fractional step method [Chorin, 1968] was used, through which the hydrostatic pressure is computed explicitly from the free surface elevation and the density field, and the nonhydrostatic pressure is determined on the condition that

¹School for Marine Science and Technology, University of Massachusetts-Dartmouth, New Bedford, Massachusetts, USA.

²Also at Marine Ecosystem and Environment Laboratory, College of Marine Science, Shanghai Ocean University, Shanghai, China.

³Department of Physical Oceanography, Woods Hole Oceanographic Institution, Woods Hole, Massachusetts, USA.

the local velocity field must be divergence-free. We have implemented both the “projection” and “pressure correction” fractional step methods [Armfield and Street, 2002] into FVCOM. In the projection method, the momentum equations are first integrated using a hydrostatic pressure gradient to obtain the intermediate velocities. This intermediate field is then corrected using the nonhydrostatic pressure gradient to produce a solenoidal velocity field [Mahadevan et al., 1996b; Marshall et al., 1997b; Casulli and Stelling, 1998; Kanarska and Maderich, 2003; Heggelund et al., 2004]. Similar to the projection method, the pressure correction method also solves the momentum equations using a fractional step approach. The key difference is that the nonhydrostatic pressure gradients are included in the first step when the intermediate velocities are determined [Stansby and Zhou, 1998; Casulli, 1999; Zijlema and Stelling, 2005; Fringer et al., 2006; Kanarska et al., 2007]. Since these two methods represent a fairly straightforward augmentation of existing hydrostatic ocean models and are relatively inexpensive in terms of computational costs, they are widely used in the development of nonhydrostatic ocean models. Methods that include the spontaneous momentum and pressure update have also been employed [Stelling and Zijlema, 2003; Yuan and Wu, 2004; Namin et al., 2001]; however, they are primarily used for inviscid surface wave problems.

[5] There arises a fundamental issue when a fractional step scheme is used to add a nonhydrostatic capability to an ocean model, which employs a split mode explicit time-stepping method. In a mode split model, an adjustment must be made at every internal time step to ensure consistency between the vertically integrated water transport produced by the external and internal modes [Mellor, 2004; Chen et al., 2006b]. For hydrostatic models, the internal velocities are adjusted to the external velocities at each time step to ensure the consistency of volume transport, since the velocities calculated by the external mode are generally more accurate than the vertically integrated velocities calculated from the internal mode. For nonhydrostatic models, however, allowing the internal velocities to be adjusted to the external velocities could be problematic, since the free surface and the 2-D velocities determined in the explicit external mode update do not have the $(n + 1)$ th time nonhydrostatic effect. For nonhydrostatic models using a semi-implicit time-stepping method, such an adjustment for velocities is not required. However, in the semi-implicit scheme, the predicted free surface elevation will be damped if the nonhydrostatic effects are not properly included in the free surface update as used in the projection method [Casulli and Stelling, 1998; Casulli, 1999].

[6] A simple solution to restoring the free surface elevation accuracy was adopted in semi-implicit nonhydrostatic models by using the pressure correction method so that the nonhydrostatic effect can be considered when solving the free surface equation (see, e.g., UNTRIM [Casulli and Zanolli, 2002] and SUNTANS [Fringer et al., 2006]). The values of the computed free surface elevations are then fixed at the end of each time step assuming the correction for $(n + 1)$ th time nonhydrostatic pressure will only exert a small change in the free surface elevation, such that the accuracy is not affected [Fringer et al., 2006]. Therefore, the pressure correction method is used in the mode split nonhydrostatic ROMS [Kanarska et al., 2007]. With this method, the non-

hydrostatic effect can be considered in the external mode. This approach appears to maintain the accuracy of the predicted external velocities, which can be used to ensure the consistency between the barotropic and baroclinic fluxes. A small error, however, could still exist in the external velocities and subsequently in the free surface elevation since the depth-integrated nonhydrostatic pressure gradients must be “frozen” over the entire external substeps [Kanarska et al., 2007].

[7] In nonhydrostatic FVCOM (hereafter FVCOM-NH), we use a different approach. First, the depth-integrated nonhydrostatic pressure gradients are always included in the external mode to give the best estimate of the free surface elevation when either the projection method or the pressure correction method is used. Second, the free surface elevation and the external velocities determined in the external mode are only regarded as intermediate values. At the end of each internal time step, the intermediate external velocities are then adjusted to the vertically integrated internal velocities. This adjustment procedure is in fact opposite of that used in the hydrostatic FVCOM. The adjusted external velocities are further used to inversely correct the intermediate free surface elevation with the inclusion of the current time step nonhydrostatic effect. Unlike UNTRIM and SUNTANS, this free surface elevation correction is also employed in the semi-implicit time-stepping FVCOM-NH to make sure that the free surface elevation exactly matches the divergent free velocity field. With these new algorithms, we have obtained a nonhydrostatic model that ensures consistency between the free surface elevation, local velocities, and the nonhydrostatic pressure field and consequently an improved capability for mass conservation.

[8] FVCOM-NH has been validated for both idealized homogeneous and stratified fluid dynamics problems. For homogeneous cases, the experiments include a surface standing wave problem in a deep flat-bottomed basin and a surface solitary wave problem in both flat-bottomed and linearly varying sloping-bottomed channels. For stratified cases, the experiments are focused on a lock exchange flow in a closed rectangular tank and internal solitary waves breaking on a sloping shelf. These selected benchmark test cases have been widely used to validate different nonhydrostatic numerical solvers. For example, the lock-exchange problem was used by Härtel et al. [2000] for spectral methods, Bourgault and Kelley [2004] (hereafter referred as B&K) and Kanarska et al. [2007] for the finite difference method, and Fringer et al. [2006] for an orthogonal unstructured grid finite volume method. The simulation of internal solitary waves represents a more realistic coastal problem to apply nonhydrostatic modeling. Since internal waves are frequently observed over steep slopes near seamounts, shelf breaks, submarine banks, and sills, where the water is stratified, it is critical to validate FVCOM-NH to assess its capability to simulate finite amplitude internal waves and robustness to reproduce the major features of the internal wave shoaling and breaking. On the basis of the excellent performance of FVCOM-NH in these test cases, we have successfully used FVCOM-NH to investigate the tidally generated large-amplitude high-frequency nonlinear internal waves observed each summer in Massachusetts Bay [Lai et al., 2010].

[9] The remainder of this paper is organized as follows. The algorithms used in solving FVCOM-NH are described in section 2, the validation experiment results are presented

in section 3, and a discussion and summary are provided in section 4.

2. Formations and Discretization Procedures of FVCOM-NH

[10] FVCOM-NH was originally coded using the σ coordinate system and has recently been modified to use the generalized terrain-following coordinate system [Pietrzak *et al.*, 2002]. The discrete approaches used to solve FVCOM-NH are the same in these two coordinates. Since the validation experiments presented in this paper were made using uniform layers in the vertical, the description given below is based on the σ coordinate version.

[11] The nonhydrostatic, free surface primitive equations in the σ coordinate transformation consist of the following momentum, continuity, temperature, salinity, and density equations given as

$$\begin{aligned} \frac{\partial uD}{\partial t} + \frac{\partial u^2D}{\partial x} + \frac{\partial uvD}{\partial y} + \frac{\partial u\omega}{\partial \sigma} - f\nu D = -gD \frac{\partial \zeta}{\partial x} - \frac{D}{\rho_0} \frac{\partial p_a}{\partial x} \\ - \frac{gD}{\rho_0} \left[\int_{\sigma}^0 D \frac{\partial \rho}{\partial x} d\sigma - \frac{\partial D}{\partial x} \int_{\sigma}^0 \sigma \frac{\partial \rho}{\partial \sigma} d\sigma \right] \\ - \frac{D}{\rho_0} \left[\frac{\partial q}{\partial x} + \frac{\partial \sigma}{\partial x} \frac{\partial q}{\partial \sigma} \right] + \frac{1}{D} \frac{\partial}{\partial \sigma} \left(K_m \frac{\partial u}{\partial \sigma} \right) + DF_u, \end{aligned} \quad (1)$$

$$\begin{aligned} \frac{\partial vD}{\partial t} + \frac{\partial uvD}{\partial x} + \frac{\partial v^2D}{\partial y} + \frac{\partial v\omega}{\partial \sigma} + fuD = -gD \frac{\partial \zeta}{\partial y} - \frac{D}{\rho_0} \frac{\partial p_a}{\partial y} \\ - \frac{gD}{\rho_0} \left[\int_{\sigma}^0 D \frac{\partial \rho}{\partial y} d\sigma - \frac{\partial D}{\partial y} \int_{\sigma}^0 \sigma \frac{\partial \rho}{\partial \sigma} d\sigma \right] \\ - \frac{D}{\rho_0} \left[\frac{\partial q}{\partial y} + \frac{\partial \sigma}{\partial y} \frac{\partial q}{\partial \sigma} \right] + \frac{1}{D} \frac{\partial}{\partial \sigma} \left(K_m \frac{\partial v}{\partial \sigma} \right) + DF_v, \end{aligned} \quad (2)$$

$$\frac{\partial wD}{\partial t} + \frac{\partial uwD}{\partial x} + \frac{\partial vwD}{\partial y} + \frac{\partial w\omega}{\partial \sigma} = -\frac{1}{\rho_0} \frac{\partial q}{\partial \sigma} + \frac{1}{D} \frac{\partial}{\partial \sigma} \left(K_m \frac{\partial w}{\partial \sigma} \right) + DF_w, \quad (3)$$

$$\frac{\partial u}{\partial x} + \frac{\partial v}{\partial y} + \frac{\partial \sigma}{\partial x} \frac{\partial u}{\partial \sigma} + \frac{\partial \sigma}{\partial y} \frac{\partial v}{\partial \sigma} + \frac{1}{D} \frac{\partial w}{\partial \sigma} = 0, \quad (4)$$

$$\frac{\partial TD}{\partial t} + \frac{\partial TuD}{\partial x} + \frac{\partial TvD}{\partial y} + \frac{\partial T\omega}{\partial \sigma} = \frac{1}{D} \frac{\partial}{\partial \sigma} \left(K_h \frac{\partial T}{\partial \sigma} \right) + D\hat{H} + DF_T, \quad (5)$$

$$\frac{\partial SD}{\partial t} + \frac{\partial SuD}{\partial x} + \frac{\partial SvD}{\partial y} + \frac{\partial S\omega}{\partial \sigma} = \frac{1}{D} \frac{\partial}{\partial \sigma} \left(K_h \frac{\partial S}{\partial \sigma} \right) + DF_S, \quad (6)$$

$$\rho = \rho(T, S, P), \quad (7)$$

where x , y , and z are Cartesian coordinates in eastward, northward, and upward directions, respectively; u , v , w are x , y , z velocity components; t is time; ω is the transformed vertical velocity in the σ coordinate; ζ is the free surface

elevation; $D = H + \zeta$; H is the static water depth; T is water temperature; S is salinity; p_a is the air pressure at the sea surface; q is the nonhydrostatic pressure; f is the Coriolis parameter; ρ is the in situ density; ρ_0 is the reference density; g is the gravity acceleration; \hat{H} is the absorption of downward shortwave irradiance; K_m is the vertical eddy viscosity; K_h is the thermal vertical eddy diffusion coefficient; and F_u , F_v , F_w , F_T , and F_S represent the horizontal diffusion terms in the momentum, thermal, and salt equations. A detailed description of the mathematical forms of the shortwave flux and horizontal diffusion terms are given in the FVCOM user manual [Chen *et al.*, 2006b].

[12] K_m and K_h are parameterized by either specified empirical formula or solving a turbulence closure model. FVCOM uses the Mellor and Yamada level 2.5 (MY-2.5) turbulence closure model [Mellor and Yamada, 1982; Galperin *et al.*, 1988] as a default setup, with the General Ocean Turbulence Model (GOTM) as an option [Burchard *et al.*, 1999; Burchard, 2002]. Horizontal diffusion coefficients are either specified as constant or calculated using Smagorinsky's turbulence closure scheme [Smagorinsky, 1963]. ω satisfies the continuity equation with the same form as that derived in the hydrostatic model [Chen *et al.*, 2003]. It is given as

$$\frac{\partial \zeta}{\partial t} + \frac{\partial uD}{\partial x} + \frac{\partial vD}{\partial y} + \frac{\partial \omega}{\partial \sigma} = 0. \quad (8)$$

P is the total pressure, i.e., the sum of the surface atmospheric pressure (p_a), hydrostatic pressure (p_H), and nonhydrostatic pressure (q), in which

$$\frac{\partial p_H}{\partial z} = -\rho g \Rightarrow p_H = \rho_0 g \zeta + g \int_z^0 \rho dz', \quad (9)$$

and q is determined by solving the pressure Poisson equation that is derived from the discrete decomposition using the fractional step method described below [Chorin, 1968].

[13] Define that u^* , v^* , and w^* are the x , y , and z components of the intermediate velocity. Then equations (1)–(3) can be discretized as

$$\frac{u^*D^* - u^nD^n}{\Delta t} = -F_x^n - a \frac{D}{\rho_0} \left(\frac{\partial q^n}{\partial x} + \frac{\partial \sigma}{\partial x} \frac{\partial q^n}{\partial \sigma} \right) + \frac{1}{D} \frac{\partial}{\partial \sigma} \left(K_m \frac{\partial u^*}{\partial \sigma} \right), \quad (10)$$

$$\frac{v^*D^* - v^nD^n}{\Delta t} = -F_y^n - a \frac{D}{\rho_0} \left(\frac{\partial q^n}{\partial y} + \frac{\partial \sigma}{\partial y} \frac{\partial q^n}{\partial \sigma} \right) + \frac{1}{D} \frac{\partial}{\partial \sigma} \left(K_m \frac{\partial v^*}{\partial \sigma} \right), \quad (11)$$

$$\frac{w^*D^* - w^nD^n}{\Delta t} = -F_z^n - a \frac{1}{\rho_0} \frac{\partial q^n}{\partial \sigma} + \frac{1}{D} \frac{\partial}{\partial \sigma} \left(K_m \frac{\partial w^*}{\partial \sigma} \right) \quad (12)$$

and

$$\frac{u^{n+1} - u^*}{\Delta t} = -\frac{1}{\rho_0} \left(\frac{\partial q'}{\partial x} + \frac{\partial \sigma}{\partial x} \frac{\partial q'}{\partial \sigma} \right), \quad (13)$$

$$\frac{\nu^{n+1} - \nu^*}{\Delta t} = -\frac{1}{\rho_0} \left(\frac{\partial q'}{\partial y} + \frac{\partial \sigma}{\partial y} \frac{\partial q'}{\partial \sigma} \right), \quad (14)$$

$$\frac{w^{n+1} - w^*}{\Delta t} = -\frac{1}{\rho_0 D} \frac{\partial q'}{\partial \sigma}, \quad (15)$$

where superscript n is an index representing the n th time step; F_x and F_y indicate the sum of advection, Coriolis, air pressure gradient, surface and hydrostatic baroclinic pressure gradients, and horizontal diffusion terms in the x and y momentum equations (1)–(2); and F_z is the sum of advection and horizontal diffusion term in the z momentum equation (3). In the right-hand side (RHS) of equations (10)–(12), D will be treated as D^n in the explicit nonhydrostatic pressure gradient term. Otherwise, it uses the intermediate value of D since the vertical diffusion terms are treated implicitly. Since the $(n+1)$ th value of D is still not available in equations (13)–(15), it is approximated by D^* and has been divided on both sides. q' is the perturbation nonhydrostatic pressure defined as

$$q^{n+1} = a \cdot q^n + q', \quad (16)$$

where a is a scalar switch that is set to zero in the projection method and to unity in the pressure correction method. With $a = 0$, the n th time step nonhydrostatic pressure gradient will not be included in the intermediate momentum update, while with $a = 1$, q^n is taken into account for the best estimate of the current time step nonhydrostatic pressure gradient. Differentiating equations (13)–(15) with respect to x , y , and z and then substituting the resulting divergence equation into equation (4), we can derive the Poisson equation for q' as

$$\begin{aligned} \frac{\partial^2 q'}{\partial x^2} + \frac{\partial^2 q'}{\partial y^2} + \left[\left(\frac{\partial \sigma}{\partial x} \right)^2 + \left(\frac{\partial \sigma}{\partial y} \right)^2 + \frac{1}{D^2} \right] \frac{\partial^2 q'}{\partial \sigma^2} \\ + 2 \left(\frac{\partial \sigma}{\partial x} \frac{\partial^2 q'}{\partial x \partial \sigma} + \frac{\partial \sigma}{\partial y} \frac{\partial^2 q'}{\partial y \partial \sigma} \right) + \left(\frac{\partial^2 \sigma}{\partial x^2} + \frac{\partial^2 \sigma}{\partial y^2} \right) \frac{\partial q'}{\partial \sigma} \\ = \frac{\rho_0}{\Delta t} \left(\frac{\partial u^*}{\partial x} + \frac{\partial \sigma}{\partial x} \frac{\partial u^*}{\partial \sigma} + \frac{\partial v^*}{\partial y} + \frac{\partial \sigma}{\partial y} \frac{\partial v^*}{\partial \sigma} + \frac{1}{D} \frac{\partial w^*}{\partial \sigma} \right) \end{aligned} \quad (17)$$

This equation is discretized using the same second-order accurate finite volume method used in the hydrostatic version of FVCOM (Appendix A). This results in the linear system

$$Aq' = b, \quad (18)$$

where A is a sparse matrix with a dimension of N_{node} (the node number) $\times K_{\text{layer}}$ (the vertical layer number) and b is a vector constructed from the right-hand side source terms in equation (17). The resulting matrix is diagonally dominant and asymmetric and can be solved efficiently using Krylov subspace methods, such as biconjugate gradient, BiCGSTAB and GMRES [Saad, 2000], in FVCOM-NH. In the present work, all the validation cases are solved by the GMRES method. Boundary conditions for equation (17) are set as follows. At the surface,

$$q' = 0; \quad (19)$$

at the bottom, a no-flux condition normal to the slope results in

$$\frac{\partial q'}{\partial \sigma} = \frac{D \tan \beta}{(1 + \tan^2 \beta)} \frac{\partial q'}{\partial n}, \quad (20)$$

where n is the unit horizontal directional vector component normal to the slope on the σ surface and β is the slope of the bottom bathymetry. At the lateral solid boundary, the no-flux condition normal to the wall is specified as

$$\frac{\partial q'}{\partial n_h} = - \left(n_x \cdot \frac{\partial \sigma}{\partial x} + n_y \cdot \frac{\partial \sigma}{\partial y} \right) \frac{\partial q'}{\partial \sigma}, \quad (21)$$

where n_h is the unit directional vector normal to the wall and n_x and n_y are the x and y components of n_h . At open boundaries, we assume that nonhydrostatic processes can be ignored by setting the RHS in equation (17) to zero or freezing the intermediate velocities. The nonhydrostatic pressure gradient at the open boundary is derived from equations (13)–(14). This approach can effectively avoid a sharp nonhydrostatic pressure gradient at the open boundary for the case when directly setting $q' = 0$.

[14] Solving the RHS of equation (17) requires the surface boundary condition for the intermediate velocity w^* . Setting $q' = 0$ within the top layer cell was proposed to avoid such a difficulty in some nonhydrostatic models. This approach, however, can cause a significant phase error for surface wave problems [Yuan and Wu, 2004; Zijlema and Stelling, 2005]. Instead of directly specifying w^* at the surface, we reconstruct the gradient of w^* in the top layer from the interior values using a fourth-order Lagrangian extrapolation method. With a more accurate gradient in w^* near the surface, the model is able to maintain q' in the top layer cell, which can be used to correct horizontal velocity components under the nonhydrostatic effect in that cell. With a corrected horizontal velocity, the final w can be updated by integrating from bottom to surface the local continuity equation. This method was employed by Fringer *et al.* [2006] to enforce a solenoidal velocity field. Since the discrete continuity equation is satisfied exactly, this method effectively avoids the potential issue that the gradient of the solution of q might not exactly satisfy the continuity equation at the discrete level in FVCOM-NH.

[15] Surface and bottom boundary conditions are required to solve equations (10)–(11) for the intermediate velocity. The horizontal momentum equations can be solved with the flux conditions determined by surface wind and bottom stresses in the same form as those in the hydrostatic model. For the vertical momentum equation, to avoid numerical errors introduced by the unknown values of u^* and v^* at the free surface and the change of ζ with time (when the discrete kinematic boundary conditions are applied), we transform the vertical velocity in the vertical diffusion terms into ω in equation (12). Since ω is zero at the surface and bottom, it allows us to simplify the vertical flux condition with a more accurate surface boundary condition.

[16] FVCOM-NH can be integrated in time using either a split mode explicit or a semi-implicit time-stepping approach. A brief description of these two methods is given in Appendix B. A major concern of nonhydrostatic models

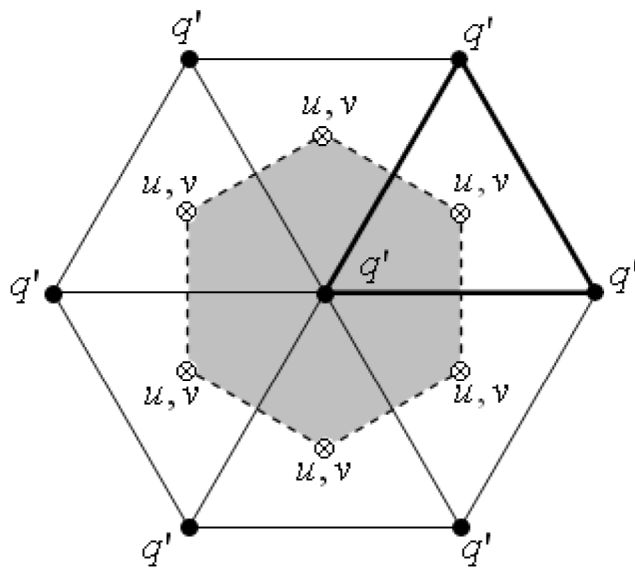


Figure 1. Schematic of the control volume for q' in the unstructured grid FVCOM-NH.

for real ocean application is the high computational cost due to the requirement of solving a large, sparse nonhydrostatic pressure matrix [Marshall *et al.*, 1997b; Kanarska *et al.*, 2007]. Three steps are used here to solve the discrete equation for q with maximum efficiency. First, FVCOM-NH is parallelized using the same efficient MPI-based framework as employed in the hydrostatic version of FVCOM [Cowles, 2008]. Second, a scalable sparse matrix solver library (PETSc) [Balay *et al.*, 2007] is implemented into the code to support the parallel computing environment for matrix solvers. Third, we employ an algebraic multigrid preconditioner using the high-performance preconditioners (HYPRE) software library [Falgout and Yang, 2002] that can be interfaced directly to the PETSc iterative solver and provides

further reduction in computational costs for solution of equation (18).

3. Validation Experiments

3.1. Surface Standing Waves in a Deep Basin

[17] Consider that a standing wave is generated by the superposition of two small amplitude surface waves that have the same period and amplitude but propagate in opposite directions. Assuming that the waveforms are along the x axis with no variation in the y direction, the governing equations for the standing wave under linear, inviscid, nonrotating conditions are

$$\frac{\partial u}{\partial t} = -\frac{1}{\rho_0} \frac{\partial p'}{\partial x}, \quad \frac{\partial w}{\partial t} = -\frac{1}{\rho_0} \frac{\partial p'}{\partial z}, \quad \text{and} \quad \frac{\partial u}{\partial x} + \frac{\partial w}{\partial z} = 0, \quad (22)$$

where $p' = \rho_0 g \zeta + q$ is the perturbation pressure as the sum of the hydrostatic pressure due to the free surface elevation and nonhydrostatic pressure q , ρ_0 is the fluid density and is assumed to have a constant value of 1000 kg/m^3 , and $g = 9.81 \text{ m/s}^2$ is the gravitational acceleration. The analytical solutions for this problem can be found in the literature [e.g., Lamb, 1945; Jankowski, 1999; Kundu and Cohen, 2002].

[18] In our case, a uninodal standing wave of free surface perturbation ($\zeta_0 = 0.1 \text{ m}$) is initiated in a closed 2-D (x - z) basin with a length of $L = 10.0 \text{ m}$ and an equilibrium depth of $H = 10.0 \text{ m}$ (Figures 1 and 2). This results in a nonhydrostatic deepwater wave, where the wavelength is the same as the local depth and the theoretical phase speed ($c = \sqrt{(g/k) \tanh(kH)}$) and period are $\sim 5.58 \text{ m/s}$ and $\sim 3.59 \text{ s}$, respectively. This case was selected mainly to examine the stability and accuracy of the split mode explicit nonhydrostatic algorithm and the nonhydrostatic pressure Poisson solver with an approximate treatment of the surface boundary condition. Because the solutions describe a periodic oscillation of an inviscid fluid within a closed domain, this case also provides a good test to examine the numerical

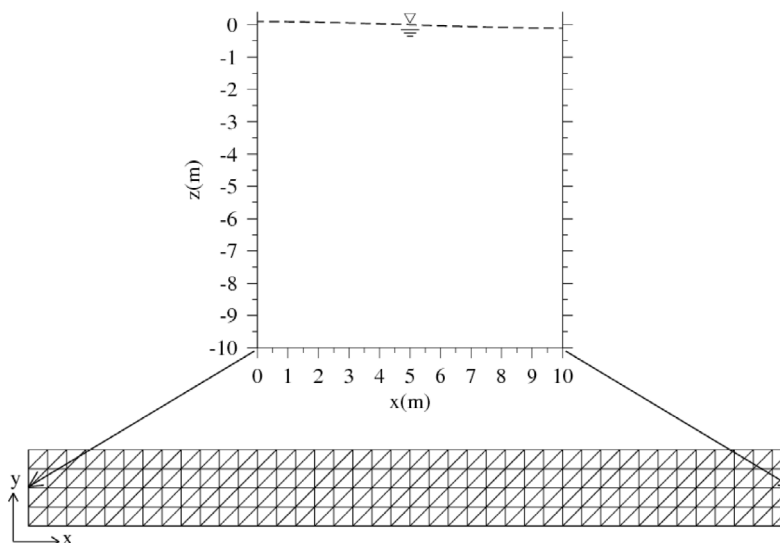


Figure 2. Schematic of the (bottom) unstructured grid and (top) vertical geometry of an idealized flat-bottomed channel used for the surface standing wave problem.

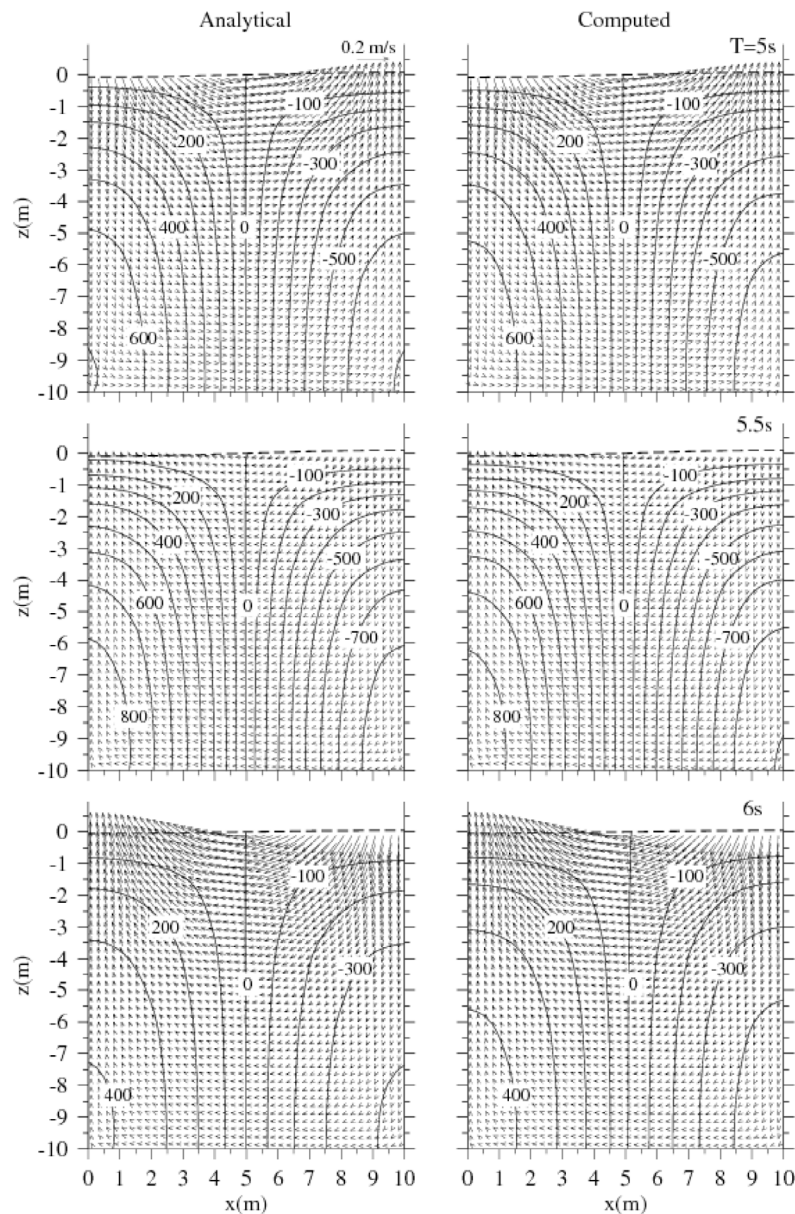


Figure 3. Sections of (left) analytical and (right) FVCOM-NH-computed solutions for the free surface elevation (dashed line), current vectors, and nonhydrostatic pressure (contours) in the x - z plane at $t = 5.0$, 5.5 , and 6.0 s.

damping and mass conservation properties of FVCOM-NH over a long-term integration.

[19] FVCOM is inherently a 3-D model. To apply it to this 2-D (x - z) problem, we configure it in a rectangular channel with a special design to ensure all variables do not vary in the y direction, which is equivalent to using the periodic boundary condition in the y direction. In this case, the domain consists of 40×4 squares in the horizontal (x - y) and 40 uniform layers in the vertical (Figure 2). The non-overlapping unstructured triangular grid in the horizontal plane is created simply by dividing each square into two triangles, with a triangle's side length of 0.25 m. Without further notification, the same triangulation and 2-D treatment has been applied to all of the following test cases. The model is integrated for 600 s using an internal mode time

step 0.05 s (also used for the nonhydrostatic pressure update) with a ratio of internal to external mode time step of 10. Using this time step, the estimated Courant number ($Cr = c\Delta t/\Delta x$) is 1.12 in this case. The model is run with an initial condition provided by the analytical solutions at $t = 0$, with a sloping free surface, zero velocity, and zero nonhydrostatic pressure. Setting $q = 0$ as the initial state is consistent with the projection method in which the nonhydrostatic pressure is not considered for the intermediate stage at the first time step. We first run the model for a linear case and then rerun it with the inclusion of the nonlinear terms. The results shown here are from the nonlinear case run, which is identical to the linear case.

[20] Figure 3 shows the comparison of model-predicted ζ , current vectors, and q with the analytical values at three

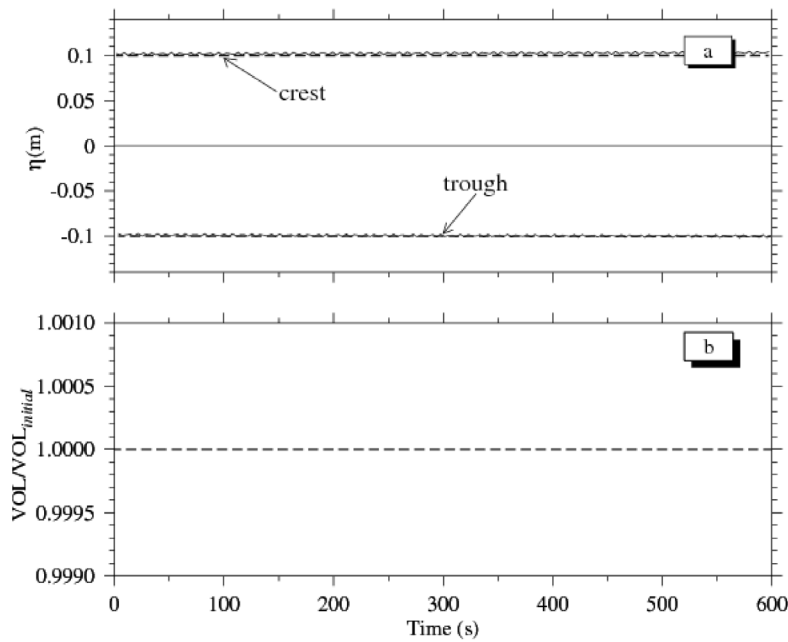


Figure 4. (a) Time series of the crest and trough of the surface standing wave at the location $x = 10$ m at the right sidewall over the 600 s integration. Heavy dashed line, analytical solution; solid line, FVCOM-NH simulation. (b) Time series of the normalized total volume in the closed domain.

select times. FVCOM-NH reproduces very closely the standing surface wave with a free surface oscillating around the nodal point in the middle of the channel and having equal maximum amplitudes on both end walls. As a result, the horizontal velocity vectors are strongest at the surface and decreases with depth, while the vertical velocity is strongest near the solid walls where the largest free surface variation is located. The pressure remains zero throughout the water column at the nodal point and increases symmetrically toward the solid end walls.

[21] The numerical damping in FVCOM-NH is insignificant in a long-term simulation. The model-predicted wave crests and troughs remain almost unchanged over the total 600 s time integration (over 160 oscillation cycles) (Figure 4a). By examining the depth integrated over the closed domain,

we find that the conservation of the model-predicted total volume (mass) is quite accurate (Figure 4b). This result demonstrates that the unstructured grid finite volume algorithm used in FVCOM-NH has excellent numerical damping properties.

[22] By analyzing the model-predicted free surface time series, we find that the new algorithm to treat the external/internal mode adjustment in mode split FVCOM-NH is highly accurate and ensures better consistency between the free surface, divergence-free velocities, and nonhydrostatic pressure field. Using the split mode explicit time-stepping and pressure correction method, the relative error of the predicted free surface is only about 1% of the analytic solution after integration over 160 periods (Figure 5 and Table 1). Even though the projection method is formally only first-

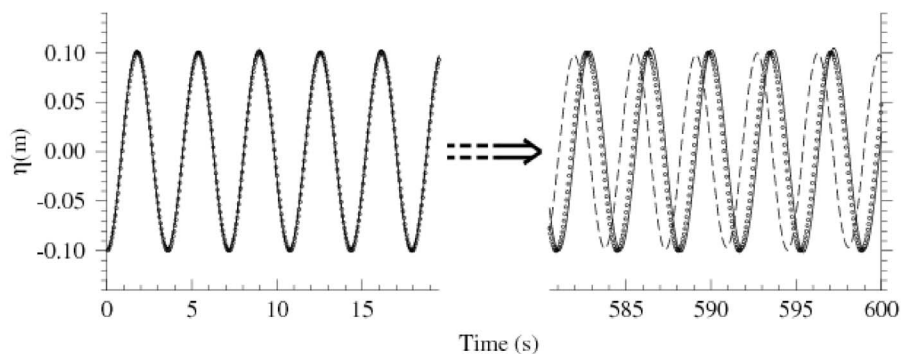


Figure 5. Comparisons of FVCOM-NH-computed and analytically derived free surface elevations with the model run under pressure correction methods for the surface standing wave problem. Circles, the analytical solution; solid line, FVCOM-NH-computed solution (nonhydrostatic runs with $q = 0$ at the surface); dashed line, FVCOM-NH-computed solutions with $q = 0$ in the top cell.

Table 1. Difference Between Model-Computed and Analytical Amplitudes and Phases of the Free Surface Elevation^a

Wave Number	Projection ($q' = 0$ at the Surface)		Correction ($q' = 0$ at the Surface)		Projection ($q' = 0$ in the Top Cell)		Correction ($q' = 0$ in the Top Cell)	
	$\Delta\zeta$ (10^{-3} m)	Δt (s)	$\Delta\zeta$ (10^{-3} m)	Δt (s)	$\Delta\zeta$ (10^{-3} m)	Δt (s)	$\Delta\zeta$ (10^{-3} m)	Δt (s)
20	1.68	0	1.69	0	2.85	-0.10	2.71	-0.10
40	2.25	0	2.17	0	0.60	-0.20	0.31	-0.20
60	-0.45	0.05	-0.53	0.05	2.30	-0.30	1.87	-0.30
80	0.40	0.05	0.34	0.05	2.23	-0.35	1.64	-0.35
100	2.19	0.10	0.20	0.05	1.50	-0.50	0.77	-0.50
120	-0.20	0.15	-0.39	0.10	3.89	-0.55	2.99	-0.55
140	-0.97	0.15	-1.07	0.15	1.48	-0.65	0.44	-0.65
160	1.60	0.20	1.37	0.20	4.75	-0.70	3.50	-0.70

^a $\Delta\zeta = \zeta_{\text{model}} - \zeta_{\text{analytic}}$ and $\Delta t = t_{\text{model}} - t_{\text{analytic}}$.

order accurate in time in contrast to the second-order time accuracy in the pressure correction method [Armfield and Street, 2002], the free surface elevations calculated using the pressure correction and pressure projection (not shown) methods agree closely with the analytical values over the entire integration (we will return to this point in the discussion). As the same free surface correction is implemented in the semi-implicit time-stepping FVCOM-NH, it also produces a similarly accurate free surface prediction using both projection and pressure correction methods as that in the mode split FVCOM-NH. Except where noted, the pressure correction method is used in the following test cases.

[23] FVCOM-NH is solved with the exact $q = 0$ at the surface through the approximation of the surface w condition in the Poisson equation. To show that this is a significant improvement over the treatment of setting $q = 0$ (or hydrostatic) within the top layer cell as used in some non-hydrostatic models, the surface standing wave case is rerun by assuming that $q = 0$ in the top layer cell. With this treatment, the model initially performs quite well in the first 45 s (~12 wave cycles) but subsequently develops a significant phase error using both pressure projection and pressure correction methods (Figure 5 and Table 1). This experiment confirms the argument by Yuan and Wu [2004] that to set $q = 0$ within the top layer cell can cause a significant phase

error in surface wave problems. The algorithm employed in the present work avoids this issue.

3.2. Surface Solitary Waves in Flat- and Sloping-Bottomed Channels

[24] The surface solitary wave is an important feature in coastal ocean dynamics. Here we validate the FVCOM-NH algorithm by investigating a propagating surface solitary wave in two geometrical settings: (1) a flat-bottomed channel and (2) a linear slope (Figure 6). In the first case, the model is compared with the analytical solution derived by Grimshaw [1971] and Fenton [1972] and summarized by Lee *et al.* [1982]. In the second case, the numerical design follows the setup of the laboratory experiment made by Madsen and Mei [1969].

3.2.1. Flat-Bottomed Case

[25] Consider an inviscid surface solitary wave travelling in a flat-bottomed channel with a length of 40.2 m, a width of 0.04 m, and a static depth of $H_0 = 0.0762$ m. The free surface elevation and the velocity fields at the initial time are generated using a third-order analytical solution for a wave amplitude of $\zeta_0 = 0.009144$ m and a ratio of $\zeta_0/H_0 = 0.12$. An effective wavelength λ is estimated by $\lambda = 6.9\sqrt{H_0^3/\zeta} = 1.52$ m, which is the double distance between the wave crest

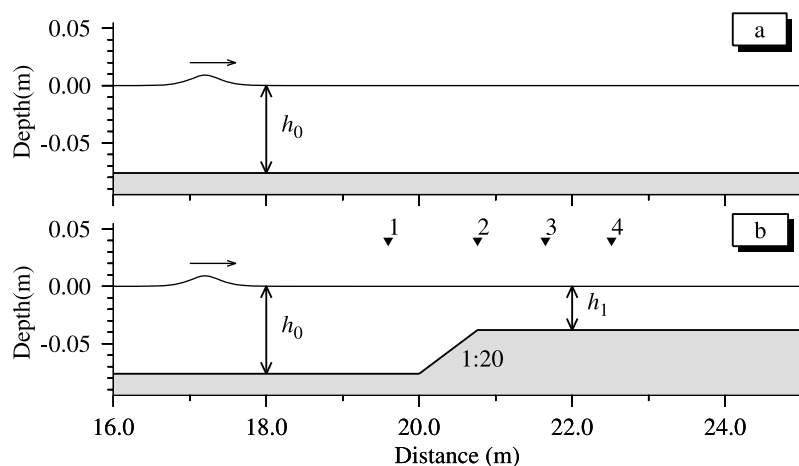


Figure 6. Sketch of geometry and initial setup of the free surface elevation in (a) flat-bottomed and (b) linear slope for the surface solitary wave problem. The length of the channel is 40.2 m, and only the middle segment between 16 and 25 m is plotted to have a clear view of the slope region. The four probe positions labeled 1–4 are shown as triangles in Figure 6b.

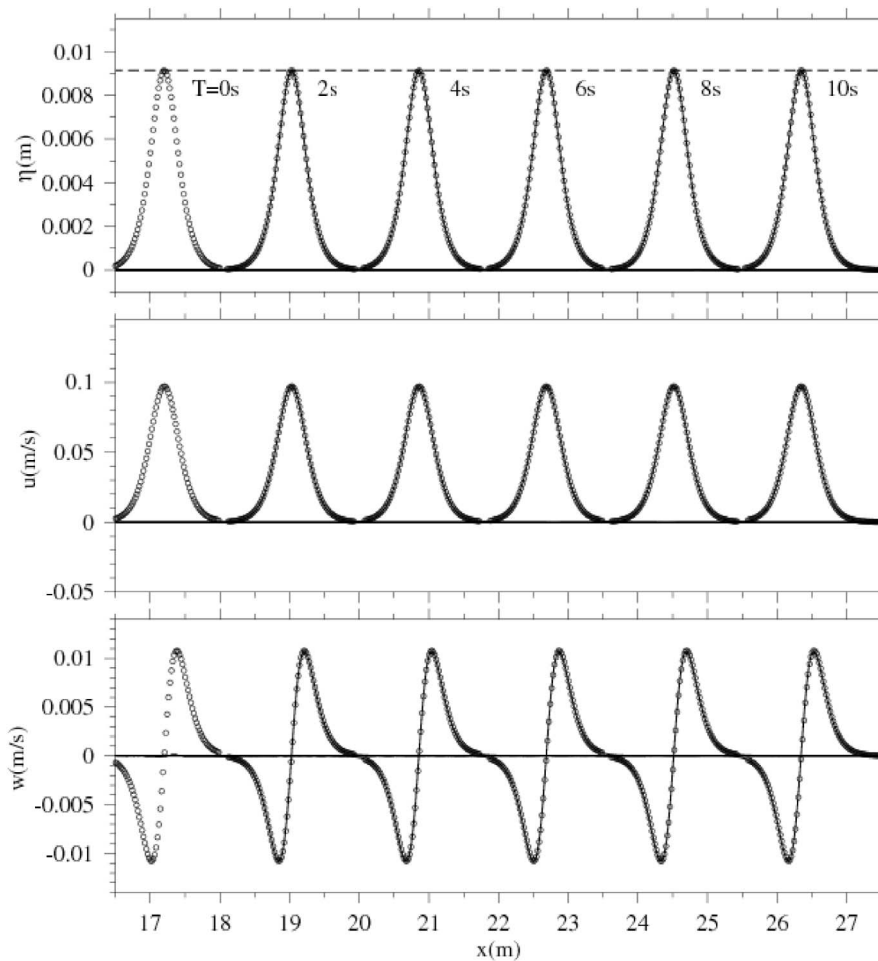


Figure 7. Comparison between FVCOM-NH-computed and analytically derived free surface elevations, along-channel velocities, and vertical velocities of the surface solitary wave at time $t = 0, 2, 4, 6, 8,$ and 10 s for the flat-bottomed case. Circles, analytic solution; solid line, FVCOM-NH; dashed line, the straight line based on the wave height at the crest at time $t = 0$.

and a point where the free surface elevation is $0.01H_0$ [Laitone, 1960; Jankowski, 1999].

[26] The computational domain uses the same mesh design as that used for the surface standing wave problem. It contains a total number of 4020×4 squares and 20 layers, which corresponds to a horizontal resolution of 0.01 m and a vertical resolution of ~ 0.003 m. In the split mode explicit approach, we chose an internal time step of 0.005 s with a ratio to the external mode time step of 10. This produces a Courant number of 0.46 and a theoretical phase speed ($c = \sqrt{g(\zeta_0 + H_0)}$) of 0.915 m/s. This setup is used in the following solitary wave test cases. The initial wave crest is set at $x = 17.2$ m (Figure 6a), and the model is integrated for 10 s, a time interval during which the wave has advanced about 9 m in the x direction and is still far enough away from the solid end wall, such that the influence from the boundary is minimal. This experiment is also repeated using the semi-implicit method using a time step of 0.05 s, and the results remain identical.

[27] FVCOM-NH reproduces the shape and propagating speed of the surface solitary wave derived from the analytical solution in inviscid conditions (Figure 7). The bal-

ance between nonlinearity and dispersion leads to a permanent free surface form symmetric around the wave crest. The largest horizontal velocity gradients are located at the middle of the wave slopes, which correspond to the location of peak vertical velocities. These features are all captured by FVCOM-NH. No obvious free surface damping is observed during the entire integration (Table 2). The excellent match of the model prediction with the analytical values on the magnitude and the phases of the horizontal and vertical velocities and the undamped amplitude of the computed wave crest demonstrate that the finite volume method used in FVCOM-NH is capable of simulating the Boussinesq-type surface solitary wave motion without explicit numerical viscosity.

3.2.2. Linear Slope Case

[28] The computational domain is the same as that used in the flat-bottomed case, except a linear slope with $dh/dx = 0.05$ (h is the height of the slope) has been added starting at $x = 20$ m (Figure 6b). H_0 and H_1 are the undisturbed water depths in the deep and shallow flat-bottomed regions, which are specified as 0.0762 and 0.0381 m, respectively. The length of the channel is set to avoid the influence of the solid end walls.

Table 2. Differences Between Analytical and Model-Predicted Values of Free Surface Elevation, Horizontal Velocity, and Absolute Vertical Velocity at Selected Simulation Times^a

Time (s)	$\Delta\zeta_{\max}$ (10^{-5} m)	Δu_{\max} (10^{-4} m/s)	$ \Delta w_{\max} $ (10^{-5} m/s)
0	0	0	0
2	0.6	3.7	1.1
4	0.2	3.4	0.9
6	-0.1	3.2	0.8
8	-0.5	3.0	0.6
10	-0.5	2.8	0.5

^aNegative sign indicates that the model value is lower than the analytical value.

[29] The same initial free surface elevation and velocity fields are used as in the flat-bottomed case, which characterizes a surface solitary wave derived from the analytical solution in the deep flat-bottomed region. The experiment made here is to examine the capability of FVCOM-NH to simulate the transformation of a solitary wave from the deep to shallow constant depth regions over a linear slope under a condition with no wave breaking.

[30] Figure 8 shows the distribution of the nondimensional free surface elevation at four probe sites labeled 1–4 (see Figure 6b) obtained from the laboratory experiment, theoretical KDV solution, and FVCOM-NH. The laboratory experiment shows that the surface solitary wave propagates from left to right, with its amplitude remaining unchanged in the deep flat-bottomed region (sites 1–2), growing over the slope (site 3), and reaching a maximum in the shallow flat region (site 4). After this single wave climbs onto the slope and enters the shallower region, it disintegrates into a wave train called a “fission phenomena.” These features are captured by FVCOM-NH. The KDV solution tends to overestimate the amplitudes of the fission wave train.

[31] Without the inclusion of bottom friction and diffusion, FVCOM-NH reproduces the laboratory experiment results. The model-predicted amplitude and phase match well with the laboratory results in the deep flat-bottomed region. When the wave climbs onto the slope, the front side of the model-predicted wave becomes steeper. The model-predicted changes of the waveshape and amplitude on the slope match well with the experimental data (Table 3). The model also resolves the fission phenomena after the water

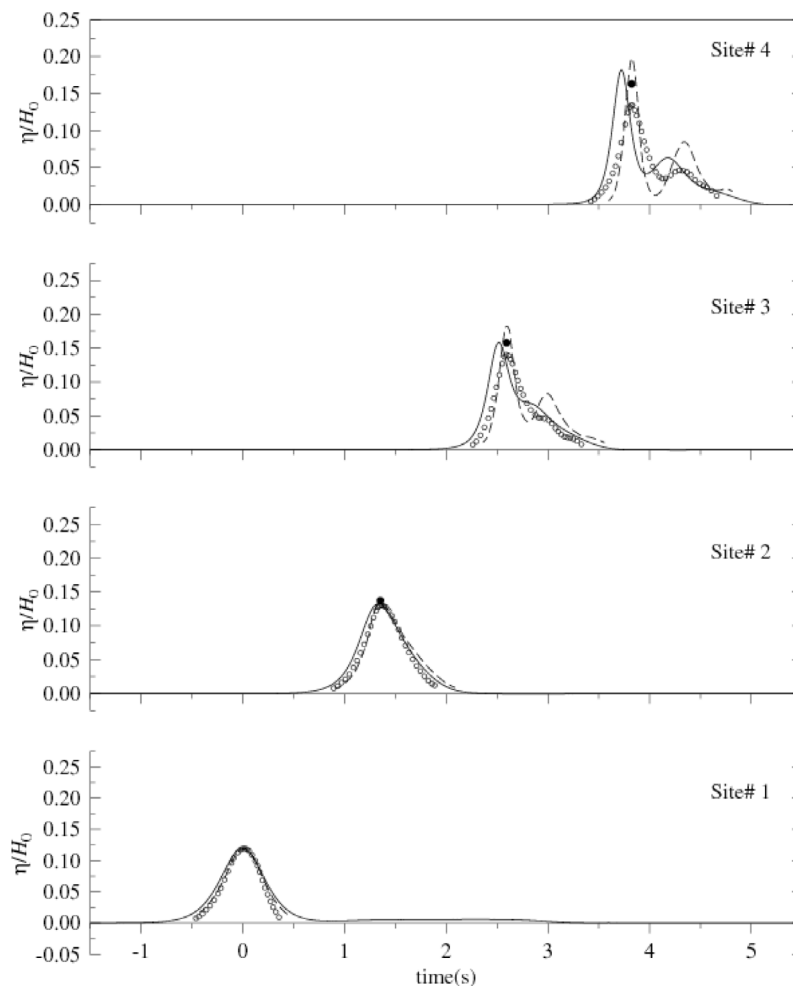


Figure 8. Comparison of the free surface elevations of the surface solitary waves predicted by FVCOM-NH (solid line), KDV theory (dashed line), and observed in the laboratory experiment (circles) at probe sites 1, 2, 3, and 4 for the linear slope case (see Figure 6 for probe positions). Solid circles, estimated free surface elevation when viscous effects shown by *Madsen and Mei* [1969]’s experiment are excluded.

Table 3. Percentage Ratio of Primary and Second Wave Heights Relative to the Initial Wave Height Calculated by FVCOM-NH, Other Nonhydrostatic Models, and Laboratory Measurements

Data Sources	Primary Wave Height/Initial Height (%)	Second Wave Height/Initial Height (%)
FVCOM-NH	152	52
<i>Madsen and Mei</i> [1969], no friction correction	112	38
<i>Madsen and Mei</i> [1969], with friction correction	136	N/A
KDV	167	75
<i>Woo and Liu</i> [2001]	150	52
<i>Hauguel</i> [1980]	163	56
<i>Yuan and Wu</i> [2004]	145	68

enters the shallower constant-depth region, which is evident at site 4. At that site, two peaks are observed. The wave heights of these two solitary waves are $\sim 152\%$ and $\sim 52\%$ as high as the initial values, respectively. These percentages are comparable with the experimental values that are 112% (without friction correction) and 136% (with friction correction) for the first crest and 38% (without friction correction) for the second crest and with other numerical model results of (150% , 52%) from *Woo and Liu* [2001], (163% , 56%) from *Hauguel* [1980], and (145% , 68%) from *Yuan and Wu* [2004], as well as with the KDV solution of (167% , 75%) (Table 3).

[32] The FVCOM-NH-computed free surface elevation, however, leads the laboratory wave by ~ 0.1 s at site 4 (Figure 8). The model-predicted phase speed is 0.24 m/s, so that the resulting space shift of the main (first) wave crest is ~ 0.024 m. Although this shift is very small, it is notable. Two possible reasons are proposed: (1) disintegration process and (2) bottom friction. We compared the disintegration process produced by the KDV solution and FVCOM-NH by overlapping the KDV-computed and FVCOM-NH-computed free surface elevation profiles at different times during the wave transformation (Figure 9). The KDV solution

shows that when the second and third solitary waves form, the leading wave decreases in wavelength but increases in wave height. Under an inviscid condition, the energy appears to be redistributed within a train of solitary waves, while its total value remains unchanged during the disintegration process. FVCOM-NH conserves the total energy during the simulation, but more energy is concentrated in the first and second solitary waves when compared with the KDV solution. As a consequence, the FVCOM-NH-predicted leading solitary wave propagates at a faster speed. Since the KDV equation is derived with the leading order approximation and solved using numerical methods, it is difficult to find the reason why the wave disintegration process found in KDV and FVCOM-NH are different.

[33] *Madsen and Mei* [1969] pointed out that their experiment was made in the laboratory with frictional damping. Using an experimental result for solitary wave damping in a flat-bottomed channel [*Ippen and Kulin*, 1955], they estimated the viscous damping height for the leading solitary wave observed at site 4. In theory, friction cannot only damp the amplitude of a wave but also retard its propagation speed, particularly after the wave enters the shallow region. To verify if the model result is sensitive to friction, we rerun the model with small constant horizontal and vertical viscosity and diffusivity of $A_m = K_h = 1 \times 10^{-6}$ m²/s and bottom friction parameterized by the bottom roughness of 0.0005 m. By adding such small viscous effects, the model-predicted phase and amplitude at site 4 become close to the experimental observations (Figure 10 and Table 3). Comparing the timing of the wave disintegration observed in FVCOM-NH runs with and without the bottom friction and diffusion, we can see that viscous effects function as a drag force to damp the wave amplitude and slow down its propagation but do not influence the timing of the transformation caused by the wave disintegration (Figure 11).

3.3. A “Lock Exchange” Problem

[34] Consider a rectangular tank filled by two fluids of different density (hereafter referred to as light and heavy)

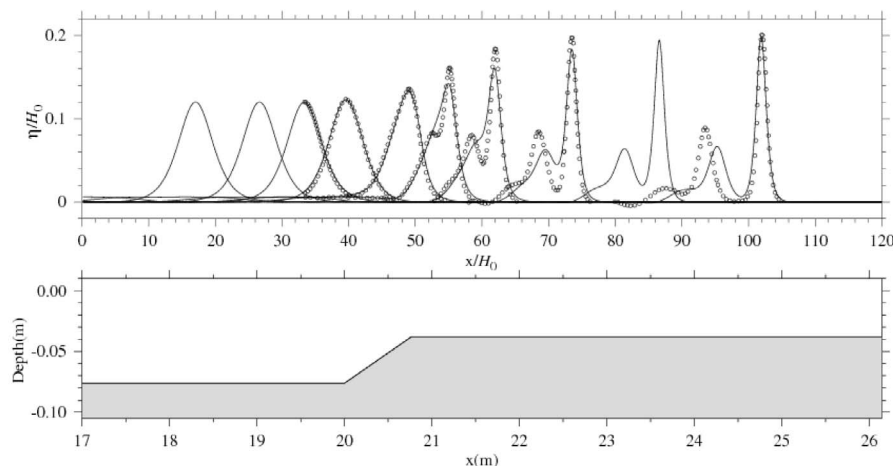


Figure 9. Transformation of FVCOM-NH-computed (solid line) and KDV-derived (circle) surface solitary waves propagating over the linear slope and onto the shallower flat-bottomed shelf under inviscid conditions.

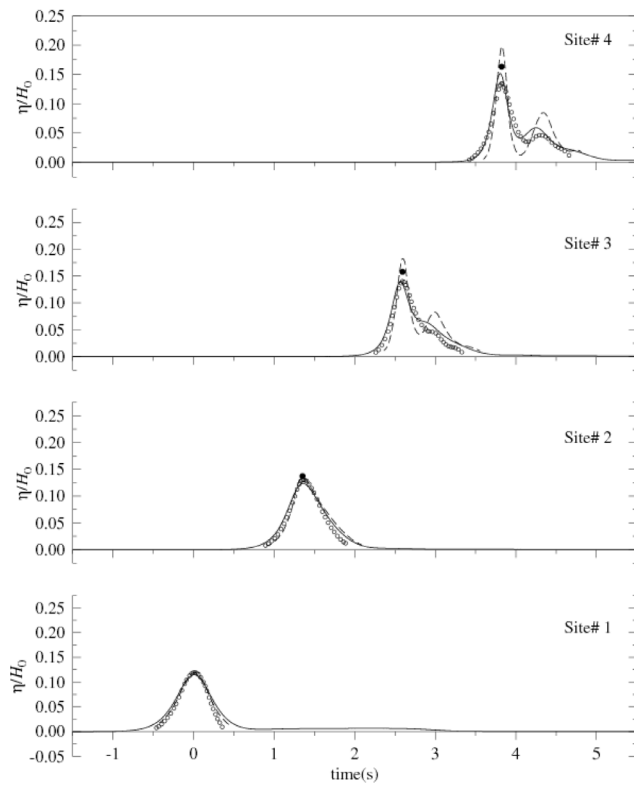


Figure 10. Comparison of free surface elevations of the surface solitary waves predicted by FVCOM-NH (solid line) with inclusion of viscous condition and observed in the laboratory experiment (circles) at probe sites 1, 2, 3, and 4 for the linear slope case. Solid circle, estimated free surface elevation when viscous effects shown by *Madsen and Mei* [1969]’s experiment are excluded.

that are separated initially by a vertical gate at the center point (Figure 12). (To compare with the previous results obtained from spectral element and unstructured grid finite volume models, we followed the same configuration as

Härtel et al. [2000] and *Fringer et al.* [2006].) The tank has a length ($L = 0.8$ m), a width ($W = 0.008$ m), and a static water depth ($H = 0.1$ m). Assuming that the density (ρ) is linearly proportional to salinity (S) given by

$$\rho = 999.972 \times (1 + 0.75 \times 10^{-3}S), \quad (23)$$

we specified the light fluid to be freshwater (with zero salinity) and the heavy fluid to be salt water with a salinity of 1.3592. Then, $\rho_1 = 999.972$ kg/m³ and $\rho_2 = 1000.991371$ kg/m³. This gives a reduced gravity (g') of

$$g' = g\Delta\rho/\rho_0 = 0.01 \text{ m/s}^2, \quad (24)$$

where ρ_0 is the reference density specified as 1000 kg/m³ and g is the gravitational acceleration constant with a value of 9.81 m/s².

[35] In the horizontal, the total number of triangles is 400 (x axis) \times 8 (y axis). In the vertical (z axis), the domain is uniformly divided into 100 layers. This configuration provides a resolution of 0.002 m in the horizontal and of about 0.001 m in the vertical. The internal time step used in this experiment is 0.003 s for the inviscid case and 0.001 s for the viscous case, with an internal-external mode split ratio of 10. Two-dimensional (x - z) flow was implemented using the methods outlined before. The model is integrated for 180 s for both inviscid and viscous (constant background molecular viscosity) conditions.

[36] The process of gravitational adjustment begins after the gate is removed at $t = 0$. The flow field is deformed from the initial state, as the heavy fluid flows underneath the lighter fluid and the velocity across the interface is of opposite sign (Figure 13). The Kelvin-Helmholtz (KH) instability appears at a time when the velocity shear between the two fluids is greater than the critical value of the restoring force determined by the density gradient. As a result of instability, a chain of well-defined vortices develops along the interface as the heads of the two fluids advance toward the end walls.

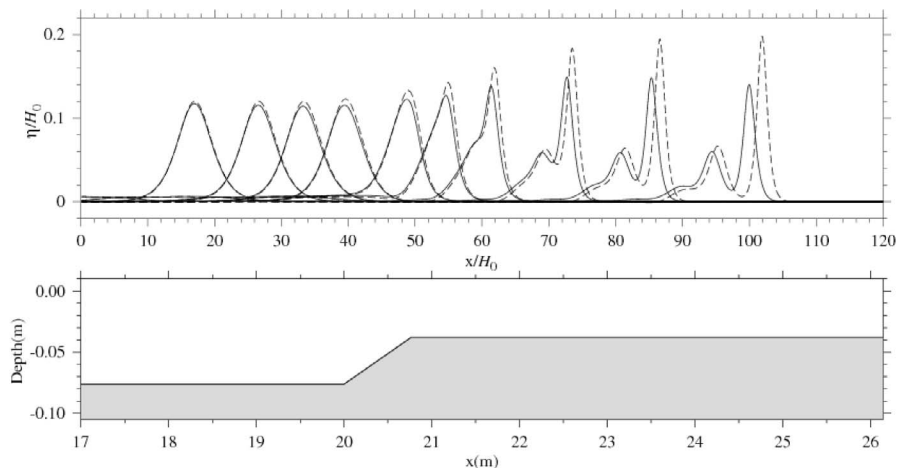


Figure 11. Transformation of FVCOM-NH-computed surface solitary waves propagating over the linear slope and onto the shallower flat-bottomed shelf under inviscid (dashed line) and viscous (solid line) conditions.

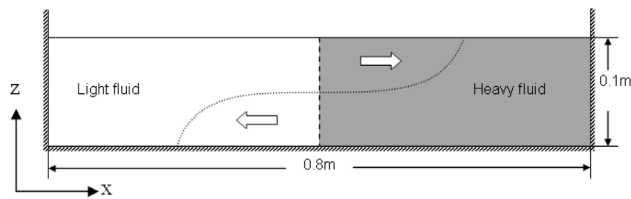


Figure 12. Schematic of lock-exchange case. Arrows presents the gravity currents, and dashed line indicates the boundary between light and heavy fluids during the initial transient.

Following the reflection from the wall, the gravity-driven water masses reverse the direction, and a complex flow field that is characterized by overturning, strong mixing, and vortices develops. The FVCOM-NH-computed evolution of the gravity current and the instability structures shown in Figure 13 is in good agreement with the laboratory experiment results described in previous literature and the comparisons with other model results given below.

[37] FVCOM-NH can run stably with no viscosity and conserve energy. The total energy of this system is defined as

$$TE = PE + KE = \int_{-L/2}^{L/2} \int_0^H \rho g z dx dz + \int_{-L/2}^{L/2} \int_0^H \frac{1}{2} \rho V (u^2 + w^2) dx dz, \quad (25)$$

where TE, PE, and KE are the total, potential, and kinetic energies, respectively, and V is the volume of an individual triangular cell. With no viscosity, TE should remain

unchanged. When the gate is removed at $t = 0$, $u = w = 0$, so that

$$\left(\int_{-L/2}^{L/2} \int_0^H \rho g z dx dz \right) \Big|_{t=0} / \int_{-L/2}^{L/2} \int_0^H \rho g z dx dz \Big|_{t=0} + \left[\int_{-L/2}^{L/2} \int_0^H \frac{1}{2} \rho V (u^2 + w^2) dx dz \right] \Big|_{t=0} / \int_{-L/2}^{L/2} \int_0^H \rho g z dx dz \Big|_{t=0} = 1, \quad (26)$$

where $\int_{-L/2}^{L/2} \int_0^H \rho g z dx dz \Big|_{t=0} = \frac{L}{4} (\rho_1 + \rho_2) g H^2 \approx 39.2589$ ($\text{kg m}^2/\text{s}^2$). Figure 14 shows the time series of the normalized dimensionless TE, PE, and KE over the integration period. The error in TE is of $O(10^{-4})$ or less (Figure 14a). After examining the spatial discretization in FVCOM-NH, we believe that the $O(10^{-4})$ error shown in the normalized TE derives from the Superbee flux limiter [Roe, 1985] implemented in the vertical advective flux calculation. This indicates that, while this limiter performs well in controlling overshooting of the flux at the interface, it has a minor influence on the energy conservation. At this error level, FVCOM-NH guarantees that the total energy of this system is conserved.

[38] FVCOM-NH predicts the correct energy transfer process in this lock exchange flow system. Starting from zero at $t = 0$, KE increases rapidly as a result of the energy transfer from PE in the first 30 s before the gravity-current head reaches the left wall (Figure 14b). Then, KE drops approximate exponentially with an increase of PE after the head hits the wall and the returning flow occurs. The inter-TK and PE transfer continues and tends to reach an equilibrium state after ~ 170 s.

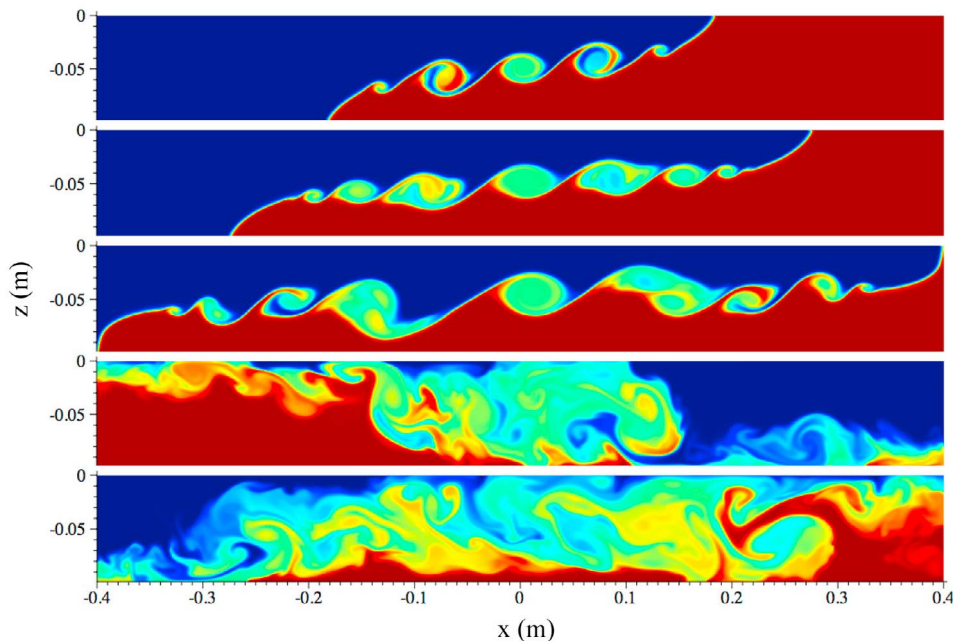


Figure 13. Density field at (top to bottom) $t = 12, 18, 27, 78,$ and 144 s after the vertical barrier is removed for the inviscid nonhydrostatic simulation.

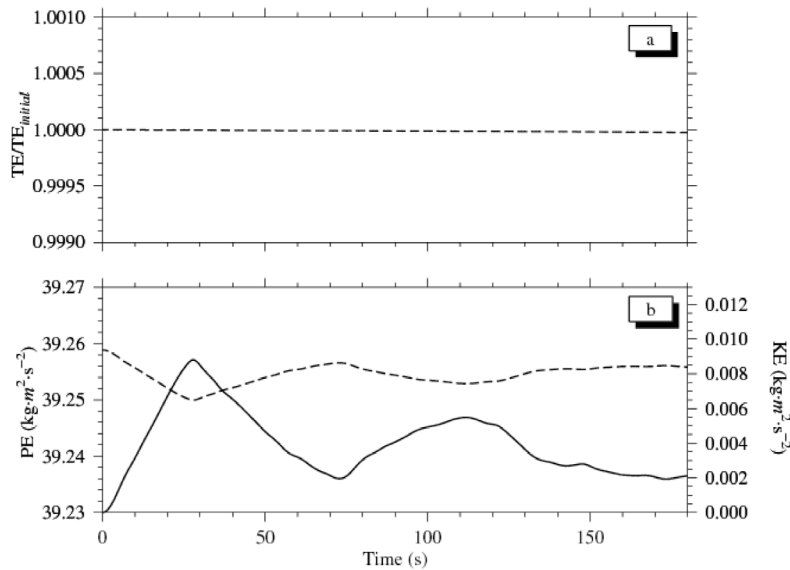


Figure 14. (a) Time series of total energy (sum of total potential and kinetic energies normalized by initial total energy) and (b) time series of total kinetic energy (KE, solid line) and total potential energy (PE, dashed line) for the inviscid flow nonhydrostatic simulation.

[39] Using the energy balance theory, *Jankowski* [1999] rederived the buoyancy velocity induced during the lock-exchange process. With no viscosity, the buoyancy velocity U is written in the form

$$U = 0.71 \sqrt{\frac{\rho_2 - \rho_1}{\rho_1 + \rho_2}} gH \approx 0.5 \sqrt{\frac{\rho_2 - \rho_1}{\rho_2}} gH = 0.5 \sqrt{g'H}, \quad (27)$$

where the reduced gravity g' is defined as $g(\rho_2 - \rho_1)/\rho_2$. Setting a measurement site at the middle point of the tank, we compare the model-predicted buoyancy velocity with equation (27). With no viscosity, the results show that before the head of the gravity current hits the wall, the maximum overflow and underflow velocities are 1.99 and 1.52 cm/s, which are slightly different from the theoretical

value of 1.59 cm/s (Figure 15a). Since the model detects a variation of free surface elevation with time and in space as well as eddies resulted from the KH instability, this is the reason why the overflow velocity is higher than the underflow velocity. To confirm this, we rerun the case with a constant value of $5 \times 10^{-6} \text{ m}^2/\text{s}$ for the horizontal and vertical diffusivity and momentum viscosity. This horizontal and vertical diffusion damps the interfacial eddies and causes the model-predicted buoyancy velocity to converge toward the analytical value (Figure 15b). This result is similar to the analysis of *B&K* to validate their laterally averaged nonhydrostatic model.

[40] FVCOM-NH is run using a free slip bottom boundary condition. To compare with the direct numerical simulation (DNS) results of *Härtel et al.* [2000], we run FVCOM-NH

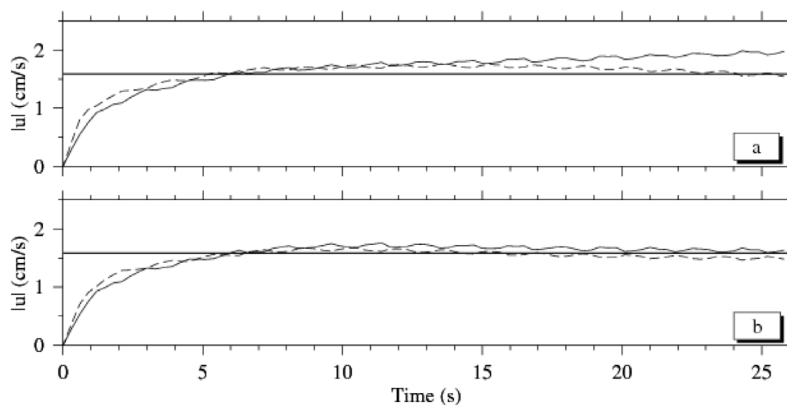


Figure 15. Time series of surface (solid line) and bottom (dashed line) horizontal velocity values measured at the midpoint of the computational domain for (a) an inviscid nonhydrostatic model simulation and (b) a nonhydrostatic model simulation with a constant value of $5 \times 10^{-6} \text{ m}^2/\text{s}$ for horizontal and vertical viscosity and diffusivity. Heavy solid line indicates the velocity value derived from the energy balance theory [Turner, 1973; Jankowski, 1999].

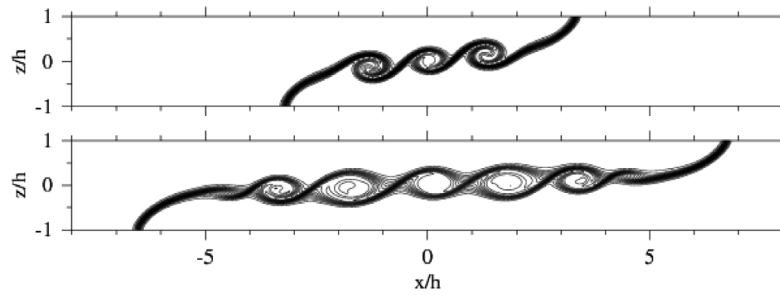


Figure 16. Distribution of the fluid density at times (top) $5T$ and (bottom) $10T$ for a nonhydrostatic model simulation with a constant background viscosity value of 10^{-6} m²/s.

with the exact same setup for the case with the Grashof number $Gr = 1.25 \times 10^{-6}$ [$Gr = (UH/2\nu)^2$, where ν is the molecular diffusivity that is specified as 10^{-6} m²/s by Härtel *et al.*'s and our experiments]. The FVCOM-NH-generated structures of interfacial vortices, shape of the intrusion front, and speed of the gravity-current head are almost identical to the DNS results. For example, Figure 16 shows the distributions of contours of density at times $5T$ and $10T$ ($T = \sqrt{D/2g'}$, $D = H + \zeta$ and ζ is the free surface elevation) after the initial transient. At both the left and right gravity current fronts, the heads intersect with the top and bottom surfaces at an angle of $\sim 60^\circ$, a similar value observed in the laboratory experiment of Turner [1973] and also in the DNS results. At $5T$, the FVCOM-NH model produces three vortices, and the left and right gravity current frontal heads are located at $x/H = -3.17$ and 3.3 , respectively. At $10T$, five vortices develop, and the left and right gravity current frontal heads move to the locations $x/H = -6.47$ and 6.7 , respectively. The vortex numbers, locations of the gravity current frontal heads, and asymmetry of the speed of the left and right gravity current frontal heads compare well with those presented in Figure 11 of Härtel *et al.* [2000].

3.4. An Internal Solitary Wave Shoaling and Breaking Problem

[41] Consider an internal solitary wave of depression propagating toward a straight beach in a rectangular domain (Figure 17). The computational domain is configured following Michallet and Ivey [1999] (hereafter referred as *M&I*) and *B&K*, with a length of 165 cm, a width of 2 cm, and a static water depth remaining constant at 15 cm from the origin to 102 cm and linearly decreasing from this position to

1.518 cm at the right end. This is a two-layer fluid system with an initial density profile given as

$$\rho = \rho_1 + \frac{\Delta\rho}{2} \left\{ 1 + \tanh \left[\frac{(z - z_i - \zeta)}{\Delta h} \right] \right\}, \quad (28)$$

where $\rho_1 = 1000$ kg/m³ is the density in the upper layer; $\Delta\rho = \rho_2 - \rho_1$, ρ_2 is the density of the lower layer; $\Delta h = 1.4$ cm is the thickness of the pycnocline; z_i is the depth of the interface; and ζ is the initial vertical displacement of the interface. The internal solitary wave was generated initially by setting ζ equal to

$$\zeta = 2a_0 \operatorname{sech}^2[(x - x_0)/2W], \quad (29)$$

where $a_0 = 3.1$ cm, x_0 is the origin, and W is the half width defined as

$$W = \frac{2h_1 h_2}{\sqrt{3a_0(h_2 - h_1)}}, \quad (30)$$

where h_1 and h_2 are the upper and lower layer thicknesses, respectively. Equation (30) is derived based on the two-layer Korteweg de Vries theory by Bogucki and Garrett [1993]. Equations (28)–(29) were directly adopted from *B&K*.

[42] We run FVCOM-NH for the two cases numbered 12 and 15 in Table 1 of *M&I*: in case I (experiment 15), $\rho_2/\rho_1 = 1.047$, $h_2/(h_1 + h_2) = 0.77$, and $W = 9.18$ cm, and in case II (experiment 12), $\rho_2/\rho_1 = 1.012$, $h_2/(h_1 + h_2) = 0.84$, and $W = 6.21$ cm. The first case is aimed at examining the general features of shoaling and breaking of the internal solitary wave, while the second case is focused on the vortex formation during breaking.

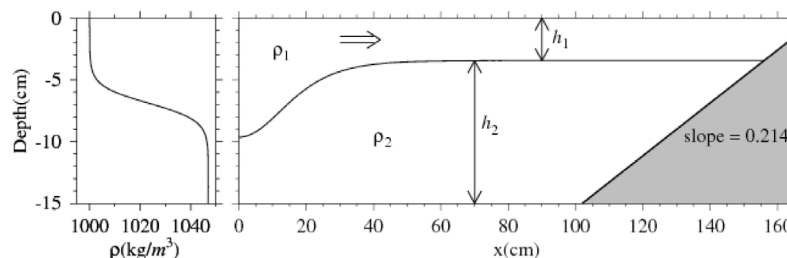


Figure 17. Schematic for the internal solitary wave shoaling and breaking case. The numerical experiment design follows Bourgault and Kelley [2004]. The variables shown in the figure are defined in the text.

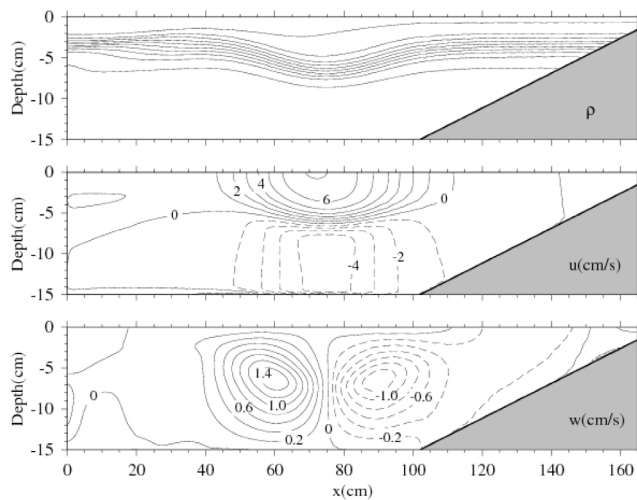


Figure 18. Distributions of (top) density, (middle) horizontal velocity, and (bottom) vertical velocity of the internal solitary wave 6.5 s after the density depression is released.

[43] This test case is configured with 240×8 triangles in the horizontal and 100 sigma layers in the vertical. The horizontal resolution was 1.0 cm in the flat-bottomed region and up to 0.5 cm over the slope. The vertical resolution varied from 0.15 cm off the slope to 0.015 cm in the shallow end of the domain. The model is run under viscous conditions with the bottom roughness specified as 0.02 cm and the viscosity and diffusivity set to a constant value of 10^{-2} cm²/s. The time step is set to 0.0005 s.

[44] With an initial interface displacement, an internal solitary wave is generated as a result of the transfer of potential energy to kinetic energy and then propagates toward the slope. The wave is characterized by a density depression, a two-layer horizontal flow with maximum onshore velocity of ~ 7 cm/s at the surface, and double cells of vertical velocity (Figure 18). For cases I and II, under the constant viscosity condition, FVCOM-NH predicts similar features of shoaling and breaking of an internal solitary wave as that shown in experiments 12 and 15 of *M&I*. Shoaling of the internal solitary wave steepens the backside of the density depression and makes the front side quickly withdraw from the slope in the offshore direction (Figure 19). Bottom friction tends to retard the fluid moving down the slope and the energy contained in the fluid moving up the slope significantly increases. Frontal instability develops and a vortex forms in the backside of the interface. Breaking occurs as a result of rapid steepening of the density profile due to intensification of the vortex (Figure 19).

[45] FVCOM-NH-computed velocity profiles in case II are in reasonably good agreement with the PIV photographs in experiment 12 of *M&I*. The laboratory experiment clearly showed a sequence of the formation and evolution of the interface vortex during shoaling. At the time at which the wave arrives on the slope, the interface is characterized by a clockwise flow in the upper layer and a relatively weak anticlockwise flow in the lower layer, where both flows converge toward the interface near the bottom (Figure 20, top left). The anticlockwise flow in the lower layer of the backside of the interface rapidly intensifies as the density

depression steepens (Figure 20, middle and bottom left). Formation and evolution of these vortices are captured in the case II experiment with constant viscosity and diffusivity by FVCOM-NH. The largest-scale feature of the vortices and the velocity amplitudes predicted by the model and observed in the laboratory experiment match reasonably well (Figure 20, right).

4. Discussion and Summary

[46] FVCOM-NH has been developed by adding non-hydrostatic dynamics into the hydrostatic version of FVCOM.

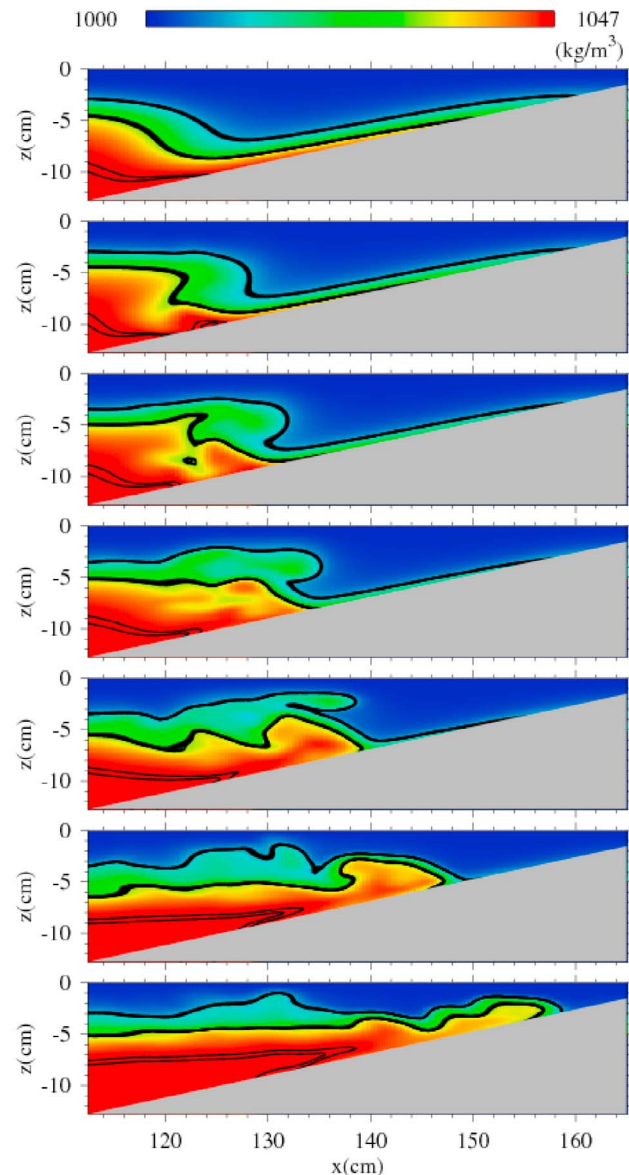


Figure 19. Sequences of snapshots of the shoaling and overturning processes of the internal solitary wave simulated by FVCOM-NH in viscous conditions. The viscous case is specified by a constant molecular diffusivity of 10^{-6} m²/s and bottom friction. The snapshots were taken at the same model time as shown in Figures 3b–3h of *Michallet and Ivey* [1999].

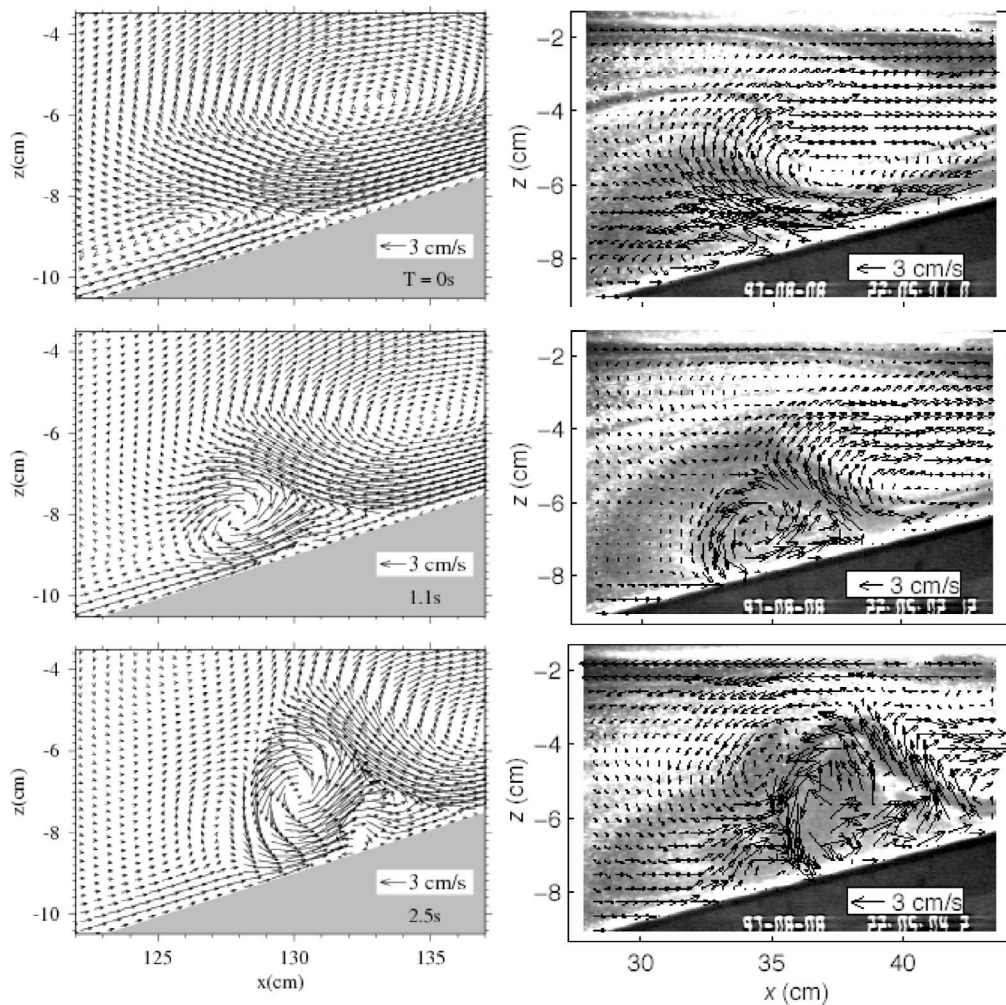


Figure 20. Comparisons between (left) FVCOM-NH-simulated and (right) laboratory-observed velocity vectors at three select times. The time listed on the bottom right corner of each frame is relative to the time at which the wave (density depression) arrives on the slope. The PIV images of the laboratory-observed velocity vector shown in *Michallet and Ivey* [1999] were kindly provided by H. Michallet, University of Grenoble, 2007. The model results used for this comparison were obtained for the case with constant molecular diffusivity and bottom friction.

A major advantage of FVCOM-NH is that this functionality is built on horizontal nonoverlapping triangular grids. Thus, the method could be optimized to solve localized small-scale nonhydrostatic phenomena in coastal and estuarine regions at the current level of computational power. UNTRIM and SUNTANS are also nonhydrostatic models that employ the unstructured grid finite volume method. FVCOM-NH differs from these models in many respects, including the discretization and grid stencils, vertical coordinate system, and the nonhydrostatic algorithms.

[47] FVCOM-NH employs a fractional step method with options for two approaches: the pressure projection and pressure correction methods. When using the split mode explicit time-stepping method, we propose a new approach to treat issues that arise when fractional step methods are used in concert with a mode splitting time-stepping framework. The sequence of steps in this new approach is in fact opposite to that used in other mode split hydrostatic and nonhydrostatic models. In our method, the free surface

determined in the external mode update will be inversely corrected by including the effect of the nonhydrostatic pressure at the current time step. This free surface correction is implemented in the semi-implicit FVCOM-NH when using either the projection or the pressure correction method. With these new treatments, we are able to establish a nonhydrostatic algorithm that ensures a consistent flow field and consequently improved mass conservation properties. On the basis of our tests, we found that the free surface fields calculated using both the projection and the pressure correction methods are quite similar regardless of whether the split mode explicit or the semi-implicit time-stepping method is used. This was somewhat surprising as the projection method is formally only first-order accurate in time while the pressure correction method is second-order accurate [Armfield and Street, 2002]. One possible reason is that in the split mode explicit scheme, FVCOM-NH includes the vertically integrated nonhydrostatic pressure gradient in the external mode in both the projection and pressure cor-

rection methods, which may improve the accuracy of the predicted intermediate velocity field and the intermediate free surface in the projection method. Correcting the free surface implicitly in both methods after obtaining the divergence-free velocity field helps correct the error in the free surface calculation, hence improving the numerical accuracy in the projection method. The same free surface correction is implemented in the semi-implicit time-stepping scheme, where it provides a similar improvement.

[48] FVCOM-NH has been validated through a set of idealized nonhydrostatic problems. The surface standing wave problem has been a benchmark test case for many other nonhydrostatic models [Casulli and Stelling, 1998; Koçyigit et al., 2002; Zijlema and Stelling, 2005; Kanarska et al., 2007]. Casulli [1999] found that the projection method used in his semi-implicit nonhydrostatic model can cause severe free surface damping. Zijlema and Stelling [2005] attributed this to the first-order accuracy error in the pressure splitting inherent in this method. For this reason, recent nonhydrostatic model development efforts prefer to use the pressure correction method [Kanarska et al., 2007; Fringer et al., 2006]. Our analysis in the surface standing wave case found that the free surface damping and mismatch found by others are probably partly attributed to their specific treatment of the surface boundary condition for q . For example, the nonhydrostatic pressure equation in UNTRIM [Casulli, 1999; Casulli and Zanolli, 2002] is solved with an assumption that $q = 0$ in the computational cell nearest the free surface. This simplification is also used in many other nonhydrostatic models [e.g., Zhou and Stansby, 1999; Stansby and Zhou, 1998; Koçyigit et al., 2002; Deponti et al., 2006]. This approach, as pointed out by Yuan and Wu [2004] and also confirmed in our experiment, can lead to a phase error in the free surface elevation. FVCOM-NH is solved with the condition of $q = 0$ at the surface, which is able to avoid the occurrence of such phase error.

[49] A nonhydrostatic version of ROMS [Haidvogel et al., 2000] has been developed recently by Kanarska et al. [2007]. Using the pressure correction method, the external mode in the nonhydrostatic version of ROMS is solved with the inclusion of nonhydrostatic pressure but with the assumption that q can be treated as a “slowly varying” force which does not vary over an internal time step. No correction is made for the free surface elevation after q and the divergence-free velocity are determined at the internal mode step. This may be the reason why the computed amplitude and phase of the surface standing wave shown by Kanarska et al. [2007] deviate from the analytical solution after 20 s (approximately four oscillation cycles), even though the grid resolution in their experiment is higher than that used in the FVCOM-NH simulation presented here. Excellent agreement between the FVCOM-NH-computed and the analytical free surface elevations in both surface standing and solitary waves in a flat-bottomed channel indicates that the variation of the nonhydrostatic pressure must be taken into account in calculating the free surface elevation in the external mode. In the split mode explicit approach, the numerical errors that occur due to fixing nonhydrostatic pressure during the external mode and artificial adjustment for 2-D to 3-D are corrected by taking the external mode field as the intermediate state and recalculating the free

surface elevation and vertically averaged velocity by solving the continuity equation with the nonhydrostatic divergence-free velocities.

[50] FVCOM-NH demonstrates conservation of total energy in inviscid conditions for the lock exchange flow problem and produces the same results for interface instability, vortex formation and evolution, and shape and speed of the gravity currents as in DNS. The lock exchange flow experiment was also performed by Fringer et al. [2006] using SUNTANS, a primitive equation ocean model which solves finite volume flux discretization on orthogonal unstructured grids. SUNTANS was run with a free surface and a no-slip bottom boundary condition. Their results were compared with the no-slip DNS results of Härtel et al. [2000], in which the no-slip condition was applied to both top and bottom boundaries. DNS results exhibit a strikingly symmetric density field, which is not present in SUNTANS simulation. The vortical structures predicted by SUNTANS also differ from the DNS results, which was attributed to the first-order upwind advection scheme used in SUNTANS [Fringer et al., 2006]. The lock exchange flow problem was also used as a benchmark test case for the nonhydrostatic version of ROMS. In a 2-D free-slip condition case, the ROMS-NH-generated vortex structures (shapes and numbers) differ significantly from results computed using DNS and FVCOM-NH.

[51] FVCOM-NH has been successfully used to capture the shoaling and breaking process of internal solitary waves observed in the laboratory. The comparison between FVCOM-NH under inviscid (not shown here) and viscous conditions suggests that the wave-breaking process and the formation of a vortex near the bottom during wave shoaling is sensitive to the bottom friction. FVCOM-NH results for the internal solitary wave case are very similar to those predicted by B&K’s nonhydrostatic finite difference model. The same experiment was also conducted using the Massachusetts Institute of Technology general circulation model (MITgcm) and the Bergen Ocean Model (BOM) by Berntsen et al. [2006]. MITgcm is a z coordinate structured grid nonhydrostatic finite volume model that uses a shaved cell approach to treat near-bottom flow over sloping-bottomed topography [Marshall et al., 1997a, 1997b], and BOM is a sigma coordinate nonhydrostatic finite difference model [Berntsen, 2000]. Berntsen et al. [2006] found that the shoaling and breaking process predicted by MITgcm in the case without bottom friction looked like BOM’s results with bottom friction. They suggest that this is probably caused by numerical errors created in the finite volume treatment of the step-bottom topography in the z coordinate model system.

[52] In summary, these validation experiments suggest that the newly developed nonhydrostatic version of FVCOM (FVCOM-NH) is capable of resolving complex nonhydrostatic phenomena in coastal and estuarine waters with high numerical accuracy, mass and energy conservation, and reasonable computational efficiency.

Appendix A: Discretization of the Poisson Equation for Nonhydrostatic Pressure

[53] The nonhydrostatic version of FVCOM (FVCOM-NH) is developed by adding a NH module into FVCOM.

The finite volume methods used to solve FVCOM-NH are the same as for FVCOM except for the Poisson equation (17) for the nonhydrostatic pressure q' . A grid convergence test based on an analytic solution of a Poisson problem in a unit square was conducted for equation (17). The results show that the log-log plot of rms error versus grid spacing has an average slope of about 2.0. This means that as grid resolution increases, the numerical error decreases at a rate of 10^{-2} , so that the solution remains at second-order accuracy as FVCOM. A detailed discussion on the accuracy of unstructured grid algorithms used in FVCOM was also given via the comparison with the structured grid finite difference model ROMSs by *Huang et al.* [2008]. In Appendix A, a brief description of the discretization of the Poisson equation is given.

[54] Equation (17) is written here as

$$\begin{aligned} & \frac{\partial^2 q'}{\partial x^2} + \frac{\partial^2 q'}{\partial y^2} + \left(A_1^2 + A_2^2 + \frac{1}{D^2} \right) \frac{\partial^2 q'}{\partial \sigma^2} \\ & + 2A_1 \frac{\partial^2 q'}{\partial x \partial \sigma} + 2A_2 \frac{\partial^2 q'}{\partial y \partial \sigma} + \left(\frac{\partial A_1}{\partial x} + \frac{\partial A_2}{\partial y} \right) \frac{\partial q'}{\partial \sigma} \\ & = \frac{\rho_0}{\Delta t} \left(\frac{\partial u^*}{\partial x} + \frac{\partial v^*}{\partial y} + A_1 \frac{\partial u^*}{\partial \sigma} + A_2 \frac{\partial v^*}{\partial \sigma} + \frac{1}{D} \frac{\partial w^*}{\partial \sigma} \right), \quad (\text{A1}) \end{aligned}$$

where $A_1 = -\frac{1}{D} \left(\frac{\partial \zeta}{\partial x} + \sigma \frac{\partial D}{\partial x} \right)$ and $A_2 = -\frac{1}{D} \left(\frac{\partial \zeta}{\partial y} + \sigma \frac{\partial D}{\partial y} \right)$. Like all other tracer variables in FVCOM, q' is placed at the nodes of each triangle (Figure 1). Defining that N ($i = 1, \dots, N$) and M ($j = 1, \dots, M$) are the total number of centroids and nodes in the computational domain and integrating equation (A1) over an individual control volume $\int \int_{\Omega_j} \int_{\sigma_k} () d\sigma dx dy$, equation (A1) can be rewritten as

$$\begin{aligned} & \oint_{l_{\Omega_j}} \left(\frac{\partial q'}{\partial x} dy - \frac{\partial q'}{\partial y} dx \right) \Delta_k(\sigma) + \overline{(A_1^2 + A_2^2 + D^{-2})} \Omega_j \Delta_k \left(\frac{\partial q'}{\partial \sigma} \right) \\ & + 2 \int_{\sigma_{k+1}}^{\sigma_k} \left(\bar{A}_1 \frac{\partial}{\partial \sigma} \oint_{l_{\Omega_j}} q' dy - \bar{A}_2 \frac{\partial}{\partial \sigma} \oint_{l_{\Omega_j}} q' dx \right) d\sigma \\ & + \left(\oint_{l_{\Omega_j}} A_1 dy \oint_{l_{\Omega_j}} A_2 dx \right) \Delta_k(q') = \frac{\rho_0}{\Delta t} \left[\left(\oint_{l_{\Omega_j}} u^* dy - \oint_{l_{\Omega_j}} v^* dx \right) \right. \\ & \left. \cdot \Delta_k(\sigma) + \bar{A}_1 \Omega_j \Delta_k(\bar{u}^*) + \bar{A}_2 \Omega_j \Delta_k(\bar{v}^*) + \frac{\Omega_j}{D} \Delta_k(\bar{w}^*) \right] \quad (\text{A2}) \end{aligned}$$

where Ω_j is the area of the control volume at the center of the j th node, k is an index of the vertical σ layer varying from 1 to k_b , Δ_k is an operator defined as the difference of the variable at k th and $(k+1)$ th σ layers, and the overbar “ $\bar{}$ ” represents the average over the area Ω_j .

[55] A_1 and A_2 are functions of $D = \zeta + H$ that are known at the $(n+1)$ th time step after the intermediate free surface elevation is determined by the external mode integration. The flux terms on the left- and right-hand sides (LHS and RHS) of equation (A2) are discretized as follows:

[56] Term 1 on LHS: Defining that

$$\begin{aligned} \Delta x_1 &= \frac{1}{2\Omega_i} (x_{i,2} - x_{i,3}); \quad \Delta x_2 = \frac{1}{2\Omega_i} (x_{i,3} - x_{i,1}); \\ \Delta x_3 &= \frac{1}{2\Omega_i} (x_{i,1} - x_{i,2}); \quad \Delta y_1 = \frac{1}{2\Omega_i} (y_{i,3} - y_{i,2}); \\ \Delta y_2 &= \frac{1}{2\Omega_i} (y_{i,1} - y_{i,3}); \quad \Delta y_3 = \frac{1}{2\Omega_i} (y_{i,2} - y_{i,1}), \end{aligned}$$

then

$$\left(\frac{\partial q'}{\partial y} \right)_{i,k+1/2} = \Delta x_1 q'_{i,k+1/2}(1) + \Delta x_2 q'_{i,k+1/2}(2) + \Delta x_3 q'_{i,k+1/2}(3); \quad (\text{A3})$$

$$\left(\frac{\partial q'}{\partial x} \right)_{i,k+1/2} = \Delta y_1 q'_{i,k+1/2}(1) + \Delta y_2 q'_{i,k+1/2}(2) + \Delta y_3 q'_{i,k+1/2}(3), \quad (\text{A4})$$

where the subscript i indicates the i th centroid, $k+1/2$ is the midlayer of k and $(k+1)$ th σ layers, 1, 2, and 3 are the indices of the three nodes of the i th triangle counted clockwise and Ω_i is the area of the i th triangle. Substituting (A3) and (A4) into the first term of equation (A2) yields

$$\begin{aligned} & \oint_{l_{\Omega_j}} \left(\frac{\partial q'}{\partial x} dy - \frac{\partial q'}{\partial y} dx \right) \Delta_k(\sigma) \\ & = \sum_{i=1}^{\text{NE}} \left\{ \left(\frac{\partial q'}{\partial x} \right)_{i,k+1/2} [dy_i(1) + dy_i(2)] \right. \\ & \quad \left. - \left(\frac{\partial q'}{\partial y} \right)_{i,k+1/2} [dx_i(1) + dx_i(2)] \right\} \Delta_k(\sigma), \quad (\text{A5}) \end{aligned}$$

where NE is the total number of triangles contained in the j th control volume with a center at the node point j , $[dx_i(1), dy_i(1)]$ and $[dx_i(2), dy_i(2)]$ represent the x and y lengths of the edge through the i th centroid for the j th control volume.

[57] Term 2 on LHS: Defining that $d\sigma(k) = \sigma(k-1/2) - \sigma(k+1/2)$, the discrete form of the second term is given as

$$\begin{aligned} & \overline{(A_1^2 + A_2^2 + D^{-2})} \Omega_j \Delta_k \left(\frac{\partial q'}{\partial \sigma} \right) = \overline{(A_1^2 + A_2^2 + D^{-2})} \Omega_j \\ & \cdot \left\{ \frac{1}{d\sigma(k)} q'_{j,k-1/2} - \left[\frac{1}{d\sigma(k)} + \frac{1}{d\sigma(k+1)} \right] \right. \\ & \left. \cdot q'_{j,k+1/2} + \frac{1}{d\sigma(k+1)} q'_{j,k+3/2} \right\}, \quad (\text{A6}) \end{aligned}$$

where the subscript j is the j th node that is the center point of the j th control volume.

[58] Term 3 on LHS: Defining that $q'_{i,k} = [q'_{i,k}(1) + q'_{i,k}(2) + q'_{i,k}(3)]/3$ in which 1, 2, and 3 are the indices of the three nodes of the i th triangle, we have

$$\begin{aligned} & 2 \int_{\sigma_{k+1}}^{\sigma_k} \left(\bar{A}_1 \frac{\partial}{\partial \sigma} \oint_{l_{\Omega_j}} q' dy - \bar{A}_2 \frac{\partial}{\partial \sigma} \oint_{l_{\Omega_j}} q' dx \right) d\sigma \\ & = 2\bar{A}_1 \sum_{i=1}^{\text{NE}} (q'_{i,k} - q'_{i,k+1}) [dy_i(1) + dy_i(2)] \\ & \quad - 2\bar{A}_2 \sum_{i=1}^{\text{NE}} (q'_{i,k} - q'_{i,k+1}) [dx_i(1) + dx_i(2)]. \quad (\text{A7}) \end{aligned}$$

Term 4 on LHS: Defining that $\bar{\sigma}_k = (\Delta_{k-1}(\sigma) + \Delta_k(\sigma))$, we have

$$\begin{aligned} & \overline{\left(\oint_{I_{\Omega_j}} A_1 dy - \oint_{I_{\Omega_j}} A_2 dx \right) \Delta_k(\bar{q}')} \\ &= \sum_{i=1}^{NE} \{ A_{1,i,k+1/2} [dy_i(1) + dy_i(2)] - A_{2,i,k+1/2} [dx_i(1) + dx_i(2)] \} \\ & \quad \cdot \left[\frac{\Delta_k(\sigma)}{\bar{\sigma}_k} q'_{i,k-1/2} + \left(\frac{\Delta_{k-1}(\sigma)}{\bar{\sigma}_k} - \frac{\Delta_{k+1}(\sigma)}{\bar{\sigma}_{k+1}} \right) \right. \\ & \quad \left. \cdot q'_{i,k+1/2} - \frac{\Delta_k(\sigma)}{\bar{\sigma}_{k+1}} q'_{i,k+3/2} \right]. \end{aligned} \quad (\text{A8})$$

Term 1 on RHS:

$$\begin{aligned} & \left(\oint_{I_{\Omega_j}} u^* dy - \oint_{I_{\Omega_j}} \nu^* dx \right) \Delta_k(\sigma) = \\ & \sum_{i=1}^{NE} \{ u^*_{i,k+1/2} [dy_i(1) + dy_i(2)] - \nu^*_{i,k+1/2} [dx_i(1) + dx_i(2)] \} \Delta_k(\sigma). \end{aligned} \quad (\text{A9})$$

Term 2 on RHS:

$$\begin{aligned} & \bar{A}_1 \Omega_j \Delta_k(\bar{u}^*) + \bar{A}_2 \Omega_j \Delta_k(\bar{\nu}^*) \\ &= \bar{A}_1 \Omega_j \left[\frac{\Delta_k(\sigma)}{\bar{\sigma}_k} u^*_{i,k-1/2} + \left(\frac{\Delta_{k-1}(\sigma)}{\bar{\sigma}_k} - \frac{\Delta_{k+1}(\sigma)}{\bar{\sigma}_{k+1}} \right) u^*_{i,k+1/2} \right. \\ & \quad \left. - \frac{\Delta_k(\sigma)}{\bar{\sigma}_{k+1}} u^*_{i,k+3/2} \right] + \bar{A}_2 \Omega_j \left[\frac{\Delta_k(\sigma)}{\bar{\sigma}_k} \nu^*_{i,k-1/2} \right. \\ & \quad \left. + \left(\frac{\Delta_{k-1}(\sigma)}{\bar{\sigma}_k} - \frac{\Delta_{k+1}(\sigma)}{\bar{\sigma}_{k+1}} \right) \nu^*_{i,k+1/2} - \frac{\Delta_k(\sigma)}{\bar{\sigma}_{k+1}} \nu^*_{i,k+3/2} \right]. \end{aligned} \quad (\text{A10})$$

Term 3 on RHS has the same form as shown in equation (A2).

[59] Substituting equations (A3)–(A10) into equation (A2) produces a set of linear equations in the form of

$$Aq' = b, \quad (\text{A11})$$

where A is a sparse coefficient matrix with a dimension of N_{node} (the node number) $\times K_{\text{layer}}$ (the vertical layer number) and b is the discrete array constructed from the right-hand side of source terms in equation (A2). The resulting matrix is diagonally dominant and asymmetric with a general form. Three steps are used to solve equation (A11). First, FVCOM-NH is parallelized using the same efficient MPI-based framework employed in the hydrostatic version of FVCOM [Cowles, 2008]. Second, a scalable sparse matrix solver library (PETSc) [Balay et al., 2007] is implemented into the code to support the parallel computing environment for matrix solvers. Third, we employ an algebraic multigrid preconditioner using the HYPRE software library [Falgout and Yang, 2002] that can be inter-

faciated directly to the PETSc iterative solver and provides further reduction in computational costs for solution of equation (A11).

Appendix B: Mode Split and Semi-Implicit Time Stepping Algorithms in FVCOM-NH

[60] In the mode split method, the governing equations for the external mode are given as

$$\frac{\partial \zeta}{\partial t} + \frac{\partial(\bar{u}D)}{\partial x} + \frac{\partial(\bar{v}D)}{\partial y} = 0, \quad (\text{B1})$$

$$\begin{aligned} & \frac{\partial \bar{u}D}{\partial t} + \frac{\partial \bar{u}^2 D}{\partial x} + \frac{\partial \bar{u} \bar{v} D}{\partial y} - f \bar{v} D - D \bar{F}_u - G_x - \frac{\tau_{sx} - \tau_{bx}}{\rho_0} \\ &= -gD \frac{\partial \zeta}{\partial x} - \frac{gD}{\rho_0} \left\{ \int_{-1}^0 \frac{\partial}{\partial x} \left(D \int_{\sigma}^0 \rho d\sigma' \right) d\sigma + \frac{\partial D}{\partial x} \int_{-1}^0 \sigma \rho d\sigma \right\} \\ & \quad + \int_{-1}^0 \left[\frac{D}{\rho_0} \left(\frac{\partial q}{\partial x} + \frac{\partial \sigma}{\partial x} \frac{\partial q}{\partial \sigma} \right) \right] d\sigma, \end{aligned} \quad (\text{B2})$$

$$\begin{aligned} & \frac{\partial \bar{v}D}{\partial t} + \frac{\partial \bar{u} \bar{v} D}{\partial x} + \frac{\partial \bar{v}^2 D}{\partial y} + f \bar{u} D - D \bar{F}_v - G_y - \frac{\tau_{sy} - \tau_{by}}{\rho_0} \\ &= -gD \frac{\partial \zeta}{\partial y} - \frac{gD}{\rho_0} \left\{ \int_{-1}^0 \frac{\partial}{\partial y} \left(D \int_{\sigma}^0 \rho d\sigma' \right) d\sigma + \frac{\partial D}{\partial y} \int_{-1}^0 \sigma \rho d\sigma \right\} \\ & \quad + \int_{-1}^0 \left[\frac{D}{\rho_0} \left(\frac{\partial q}{\partial y} + \frac{\partial \sigma}{\partial y} \frac{\partial q}{\partial \sigma} \right) \right] d\sigma, \end{aligned} \quad (\text{B3})$$

where the definition of G_x and G_y are given by Chen et al. [2003]; (τ_{sx}, τ_{sy}) and (τ_{bx}, τ_{by}) are the x and y components of surface wind and bottom stresses, respectively; and the overbar denotes vertical integration.

[61] Equations (B1)–(B2) are solved using the modified fourth-order Runge-Kutta time-stepping scheme as in FVCOM [Chen et al., 2003, 2006b]. This is a modified four-stage time-stepping method with second-order accuracy [Dick, 1994]. Over the four-stage integration from n to $n+1$, q is given by its value at the n th time step and remains unchanged. Because of the lack of variation of q during the integration, the free surface elevation and vertically integrated velocity at the $(n+1)$ th time step are treated as the intermediate values and then corrected inversely through the 2-D to 3-D adjustment after q and the nonhydrostatic 3-D velocity at the $(n+1)$ th time step are determined.

[62] The external and internal mode consistency adjustment in FVCOM-NH is treated differently from the procedure used in the hydrostatic version of FVCOM. Under the hydrostatic approximation, with shorter time step, \bar{u} and \bar{v} calculated by the external mode are more accurate than $1/D \int_{-H}^{\zeta} u dz$ and $1/D \int_{-H}^{\zeta} v dz$ calculated from the internal mode. In this case, the internal velocity is adjusted to the external velocity at each time step to ensure the mode split consistency [Chen et al., 2006b]. Under the nonhydrostatic approximation, however, the external mode only provides

the intermediate free surface elevation for the use in determining the surface boundary condition of w and total water depth at the intermediate time step in the pressure Poisson equation. The true free surface elevation and (\bar{u}, \bar{v}) at the $(n + 1)$ th time step is determined inversely by the divergence-free velocities (u, v, w) under the fully non-hydrostatic condition as follows. First, define

$$\bar{u}^{n+1} = \int_{-1}^0 u^{n+1} d\sigma \text{ and } \bar{v}^{n+1} = \int_{-1}^0 v^{n+1} d\sigma. \quad (\text{B4})$$

Second, substituting \bar{u}^{n+1} and \bar{v}^{n+1} into the continuity equation (B1), we can obtain ζ^{n+1} by solving a fully implicit discrete equation given as

$$\frac{\zeta^{n+1} - \zeta^n}{\Delta t} + \frac{\partial[\bar{u}^{n+1}(H + \zeta^{n+1})]}{\partial x} + \frac{\partial[\bar{v}^{n+1}(H + \zeta^{n+1})]}{\partial y} = 0. \quad (\text{B5})$$

Equation (B5) results in a 2-D asymmetric and diagonally dominant matrix with a stencil equal to the sum of the surrounding node points contained in a control volume, which can be solved efficiently.

[63] This approach avoids the artificial adjustment that is required in the hydrostatic version of FVCOM or other time-split models. Because the true values of ζ^{n+1} , \bar{u}^{n+1} , and \bar{v}^{n+1} are determined using the 3-D divergence-free velocity under the fully nonhydrostatic conditions, the volume fluxes for internal and external modes are matched exactly.

[64] In the semi-implicit time-stepping method, we follow the algorithm used by *Casulli and Cattani* [1994]. The horizontal momentum equations (1)–(2) are given as

$$\begin{aligned} \frac{\partial u D}{\partial t} + \frac{\partial u^2 D}{\partial x} + \frac{\partial uv D}{\partial y} + \frac{\partial u \omega}{\partial \sigma} - fv D = -gD \left[(1 - \theta) \frac{\partial \zeta^n}{\partial x} + \theta \frac{\partial \zeta^{n+1}}{\partial x} \right] \\ - \frac{D}{\rho_0} \frac{\partial p_a}{\partial x} - \frac{gD}{\rho_0} \left[\int_{\sigma}^0 D \frac{\partial \rho}{\partial x} d\sigma - \frac{\partial D}{\partial x} \int_{\sigma}^0 \sigma \frac{\partial \rho}{\partial \sigma} d\sigma \right] \\ - \frac{D}{\rho_0} \left(\frac{\partial q}{\partial x} + \frac{\partial \sigma}{\partial x} \frac{\partial q}{\partial \sigma} \right) + \frac{1}{D} \frac{\partial}{\partial \sigma} \left(K_m \frac{\partial u}{\partial \sigma} \right) + DF_u, \end{aligned} \quad (\text{B6})$$

$$\begin{aligned} \frac{\partial v D}{\partial t} + \frac{\partial uv D}{\partial x} + \frac{\partial v^2 D}{\partial y} + \frac{\partial v \omega}{\partial \sigma} + fu D = -gD \left[(1 - \theta) \frac{\partial \zeta^n}{\partial y} + \theta \frac{\partial \zeta^{n+1}}{\partial y} \right] \\ - \frac{D}{\rho_0} \frac{\partial p_a}{\partial y} - \frac{gD}{\rho_0} \left[\int_{\sigma}^0 D \frac{\partial \rho}{\partial y} d\sigma - \frac{\partial D}{\partial y} \int_{\sigma}^0 \sigma \frac{\partial \rho}{\partial \sigma} d\sigma \right] \\ - \frac{D}{\rho_0} \left(\frac{\partial q}{\partial y} + \frac{\partial \sigma}{\partial y} \frac{\partial q}{\partial \sigma} \right) + \frac{1}{D} \frac{\partial}{\partial \sigma} \left(K_m \frac{\partial v}{\partial \sigma} \right) + DF_v, \end{aligned} \quad (\text{B7})$$

in which the free surface gradient is given by a weight average of its values at n th and $(n + 1)$ th time steps. In this approach, the continuity equation is defined as

$$\begin{aligned} \frac{\partial \zeta}{\partial t} + (1 - \theta) \frac{\partial(\bar{u}D)^n}{\partial x} + \theta \frac{\partial(\bar{u}D)^{n+1}}{\partial x} \\ + (1 - \theta) \frac{\partial(\bar{v}D)^n}{\partial y} + \theta \frac{\partial(\bar{v}D)^{n+1}}{\partial y} = 0. \end{aligned} \quad (\text{B8})$$

Rewrite equations (B6)–(B7) as

$$\frac{\partial u D}{\partial t} = \text{XFLUX}^n - g\theta D \frac{\partial \zeta^{n+1}}{\partial x} + \frac{1}{D} \frac{\partial}{\partial \sigma} \left(K_m \frac{\partial u}{\partial \sigma} \right), \quad (\text{B9})$$

$$\frac{\partial v D}{\partial t} = \text{YFLUX}^n - g\theta D \frac{\partial \zeta^{n+1}}{\partial y} + \frac{1}{D} \frac{\partial}{\partial \sigma} \left(K_m \frac{\partial v}{\partial \sigma} \right), \quad (\text{B10})$$

where XFLUX and YFLUX are the sum of all explicit terms of advection, free surface gradient, atmospheric pressure gradient, hydrostatic and nonhydrostatic pressure gradients, Coriolis force, and horizontal diffusion in the x and y momentum equations, respectively.

[65] Integrating equations (B9)–(B10) from $\sigma = -1$ to $\sigma = 0$ yields

$$\begin{aligned} (\bar{u}D)^{n+1} = (\bar{u}D)^n + \Delta t \int_{-1}^0 \text{XFLUX}^n d\sigma - g\theta D \Delta t \frac{\partial \zeta^{n+1}}{\partial x} \\ + \Delta t \frac{\tau_{sx}^n - \tau_{bx}^n}{D}, \end{aligned} \quad (\text{B11})$$

$$\begin{aligned} (\bar{v}D)^{n+1} = (\bar{v}D)^n + \Delta t \int_{-1}^0 \text{YFLUX}^n d\sigma - g\theta D \Delta t \frac{\partial \zeta^{n+1}}{\partial y} \\ + \Delta t \frac{\tau_{sy}^n - \tau_{by}^n}{D}, \end{aligned} \quad (\text{B12})$$

where $(\tau_{sx}^n, \tau_{sy}^n)$ and $(\tau_{bx}^n, \tau_{by}^n)$ are the n th time x and y components of surface wind and bottom stresses, respectively. Substituting equations (B11)–(B12) into equation (B8) produces a 2-D asymmetric and diagonally dominant matrix similar to that produced by equation (B5) for the inverse free surface updating in the split mode explicit method. This matrix is solved using PETSc with preconditional HYPRE software library.

[66] After ζ^{n+1} is calculated, substituting it into equations (B9)–(B10), we can update the $(n + 1)$ th velocity by solving it implicitly for the vertical diffusion terms. Like the split mode explicit method, we also inversely correct the free surface based on equation (B8) after the $(n + 1)$ th divergence-free velocity field is updated by the nonhydrostatic pressure q' .

[67] **Acknowledgments.** This research was supported by NOAA grants DOC/NOAA/NA04NMF4720332 and DOC/NOAA/NA05NMF4721131; US GLOBEC Northwest Atlantic/Georges Bank Program NSF grants OCE-0234545, OCE-0227679, OCE-0606928, OCE-0712903, OCE-0732084, and OCE-0726851; MIT sea grant 2006-RC-103; and NOAA NERACOOS grant NA100558 for the UMASSD team and the Smith Chair in Coastal Oceanography and NOAA grant NA-17RJ1223 for R.C. Beardsley. C. Chen's contribution is also supported by Shanghai Ocean University International Cooperation Program (A-2302-10-0003), the Program of Science and Technology Commission of Shanghai Municipality (09320503700), the Leading Academic Discipline Project of Shanghai Municipal Education Commission (Project J50702), and Zhi jiang Scholar and 111 project funds of the State Key Laboratory for Estuarine and Coastal Research, East China Normal University. We would like to thank H. Michallet and C. N. Ivey for providing us with a clear PIV image from their experiments for our model data comparison. The authors would also like to thank the reviewers whose comments have done much to improve the manuscript. We want to thank the FVCOM development team members in the Marine Ecosystem Dynamics and Modeling Laboratory, School of Marine Science and Technology, UMASSD for their support and assistance in updating and improving the FVCOM code.

We would also like to thank B. Rothschild for his continuous support in the development of FVCOM-NH. This paper is 10-1001 in the SMAST Contribution Series, School of Marine Science and Technology, University of Massachusetts-Dartmouth and the US GLOBEC contribution number 686.

References

- Armfield, S., and R. Street (2002), An analysis and comparison of the time accuracy of fractional step methods for the Navier-Stokes equations on staggered grids, *Int. J. Numer. Methods Fluids*, 38(3), 255–282.
- Balay, S., K. Buschelman, V. Eijkhout, W. Group, D. Kaushik, M. Knepley, L. G. McInnes, B. Smith, and H. Zhang (2007), *PETSc User Manual*, 190 pp., *Tech. Rep. ANL-95/11-Revision 2.3.3*, Math. Comput. Sci. Div., Argonne National Lab.
- Beji, S., and J. A. Battjes (1994), Numerical simulation of nonlinear wave propagation over bar, *Coast. Eng.*, 23, 1–16.
- Berntsen, J. (2000), *Users Guide for a Mode Split S Coordinate Numerical Ocean Model*, 48 pp., *Tech. Rep. 135*, Dep. Appl. Math., Univ. of Bergen, Bergen, Norway.
- Berntsen, J., J. Xing, and G. Alendal (2006), Assessment of nonhydrostatic ocean models using laboratory scale problems, *Cont. Shelf Res.*, 26, 1433–1447.
- Bogucki, D., and C. Garrett (1993), A simple model for shear-induced decay of an internal solitary wave, *J. Phys. Oceanogr.*, 23, 1767–1776.
- Bourgault, D., and D. E. Kelley (2004), A laterally averaged nonhydrostatic ocean model, *J. Atmos. Ocean. Tech.*, 21, 1910–1924.
- Burchard, H. (2002), *Applied turbulence modeling in marine waters, Lecture Notes in Earth Sciences 100*, 215 pp., Springer, Berlin.
- Burchard, H., K. Bolding, and M. R. Villarreal (1999), *GOTM-A General Ocean Turbulence Model, Theory, Applications and Test Cases*, 103 pp., EUR 18745 EN, European Commission (European Union), Brussels, Belgium.
- Casulli, V. (1999), A semi-implicit finite difference method for nonhydrostatic free surface flows, *Int. J. Numer. Methods Fluids*, 30, 425–440.
- Casulli, V., and E. Cattani (1994), Stability, accuracy and efficiency of a semi-implicit method for three-dimensional shallow water flow, *Comput. Math. Appl.*, 27(4), 99–112.
- Casulli, V., and G. S. Stelling (1998), Numerical simulation of 3-D quasi-hydrostatic, free surface flows, *J. Hydraul. Eng.*, 124, 678–686.
- Casulli, V., and P. Zanolli (2002), Semi-implicit numerical modeling of nonhydrostatic free surface flows for environmental problems, *Math. Comput. Model.*, 36(9–10), 1131–1149.
- Chen, C., H. Liu, and R. C. Beardsley (2003), An unstructured, finite volume, three-dimensional, primitive equation ocean model: Application to coastal ocean and estuaries, *J. Atmos. Ocean. Tech.*, 20(1), 159–186.
- Chen, C., R. C. Beardsley, and G. Cowles (2006a), An unstructured grid, finite volume coastal ocean model (FVCOM) system. Special issue entitled “Advances in Computational Oceanography,” *Oceanography*, 19(1), 78–89.
- Chen, C., R. C. Beardsley, and G. Cowles (2006b), An unstructured grid, finite volume coastal ocean model FVCOM user manual. SMAST/UMASSD, 2006.
- Chen, C., H. Huang, R. C. Beardsley, H. Liu, Q. Xu, and G. Cowles (2007), A finite volume numerical approach for coastal ocean circulation studies: Comparisons with finite difference models, *J. Geophys. Res.*, 112, C03018, doi:10.1029/2006JC003485.
- Chorin, A. J. (1968), Numerical solution of Navier-Stokes equations, *Math. Comput.*, 22, 745–762.
- Cowles, G. (2008), Parallelization of the FVCOM coastal ocean model, *Int. J. High Perform. Comput. Appl.*, 22(2), 177–193.
- Deponi, A., V. Pennati, and L. De Biase (2006), A fully 3-D finite volume method for incompressible Navier-Stokes equations, *Int. J. Numer. Methods Fluids*, 52(6), 617–638.
- Dick, E. (1994), Introduction to finite volume techniques in computational fluid dynamics, in *Computational Fluid Dynamics*, edited by J. F. Wendt, pp. 271–297, Springer.
- Falgout, D. R., and U. M. Yang (2002), Hypre: A library of high performance preconditioners, in *Computational Science-ICCS 2002 Part III, Lecture Notes in Computer Science 2331*, edited by P. M. A. Sloot et al., pp. 632–641, Springer.
- Fenton, J. (1972), A ninth-order solution for the solitary wave, *J. Fluid Mech.*, 53(2), 257–271.
- Fringer, O. B., M. Gerritsen, and R. L. Street (2006), An unstructured grid, finite volume, nonhydrostatic, parallel coastal ocean simulator, *Ocean Modell.*, 14, 139–173.
- Galperin, B., L. H. Kantha, S. Hassid, and A. Rosati (1988), A quasi-equilibrium turbulent energy model for geophysical flows, *J. Atmos. Sci.*, 45, 55–62.
- Gerkema, T. (2001), Internal and interfacial tides: Beam scattering and local generation of solitary waves, *J. Mar. Res.*, 59, 227–255.
- Grimshaw, R. (1971), The solitary wave in water of variable depth: Part 2, *J. Fluid Mech.*, 46(3), 611–622.
- Haidvogel, D. B., H. G. Arango, K. Hedstrom, A. Beckmann, P. M. Rizzoli, and A. F. Schepetkin (2000), Model evaluation experiments in the North Atlantic Basin, simulation in nonlinear terrain-following coordinates, *Dyn. Atmos. Oceans*, 32, 239–281.
- Härtel, C., E. Meiburg, and F. Necker (2000), Analysis and direct numerical simulation of the flow at a gravity-current head: Part 1. Flow topology and front speed for slip and no-slip boundaries, *J. Fluid Mech.*, 418, 189–212.
- Hauguel, A. (1980), Adaptation of tidal numerical models to shallow water wave problems, in Proc. 17th Coast. Eng. Conf., Sydney, Aust.
- Heggelund, Y., F. Vikebo, J. Bernsten, and G. Furnes (2004), Hydrostatic and nonhydrostatic studies of gravitational adjustment over a slope, *Cont. Shelf Res.*, 24, 2133–2148.
- Huang, H., C. Chen, G. W. Cowles, C. D. Winant, R. C. Beardsley, K. S. Hedstrom, and D. B. Haidvogel (2008), FVCOM validation experiments: Comparisons with ROMS for three idealized barotropic test problems, *J. Geophys. Res.*, 113, C07042, doi:10.1029/2007JC004557.
- Ippen, A. T., and G. Kulin (1955), Shoaling and breaking characteristics of the solitary wave, *MIT Hydro. Lab. Tech. Rep.* 15.
- Jankowski, J. A. (1999), A nonhydrostatic model for free surface flows, Ph. D. dissertation, 251 pp., Univ. of Hannover, Germany.
- Jones, H., and J. Marshall (1993), Convection with rotation in a neutral ocean: A study of open-ocean deep convection, *J. Phys. Oceanogr.*, 23, 1009–1039.
- Kanarska, Y., and V. Maderich (2003), A nonhydrostatic numerical model for calculating free surface stratified flows, *Ocean Dyn.*, 53(3), 176–185.
- Kanarska, Y., A. Schepetkin, and J. C. McWilliams (2007), Algorithm for nonhydrostatic dynamics in the regional oceanic modeling system, *Ocean Modell.*, 18, 143–174.
- Kocycigit, M., R. Falconer, and B. Lin (2002), Three-dimensional numerical modeling of free surface flows with nonhydrostatic pressure, *Int. J. Numer. Methods Fluids*, 40(9), 1145–1162.
- Kundu, P. K., and I. M. Cohen (2002), *Fluid Mechanics*, 2nd ed, Academic, San Diego, Calif.
- Lai, Z., C. Chen, G. W. Cowles, and R. C. Beardsley (2010), Nonhydrostatic version of FVCOM: 2. Mechanistic study of tidally generated nonlinear internal waves in Massachusetts Bay, *J. Geophys. Res.*, doi:10.1029/2010JC006331, in press.
- Laitone, E. (1960), The second approximation to cnoidal and solitary waves, *J. Fluid Mech.*, 9, 430–444.
- Lamb, H. (1945), *Hydrodynamics*, 6th ed, Dover, New York.
- Lee, J. J., E. Skjelbreia, and F. Raichlen (1982), Measurement of velocities in solitary waves, *J. Waterw. Port Coastal Ocean Div.*, 108(2), 200–218.
- Madsen, O. S., and C. C. Mei (1969), The transformation of a solitary wave over an uneven bottom, *J. Fluid Mech.*, 39(4), 781–791.
- Mahadevan, A., J. Oliger, and R. Street (1996a), A nonhydrostatic meso-scale ocean model: Part I. Well-posedness and scaling, *J. Phys. Oceanogr.*, 26, 1868–1880.
- Mahadevan, A., J. Oliger, and R. Street (1996b), A nonhydrostatic meso-scale ocean model: Part II. Numerical implementation, *J. Phys. Oceanogr.*, 26, 1881–1900.
- Marshall, J., C. Hill, L. Perelman, and A. Adcroft (1997a), A hydrostatic, quasi-hydrostatic, and nonhydrostatic ocean modeling, *J. Geophys. Res.*, 102(C3), 5733–5752, doi:10.1029/96JC02776.
- Marshall, J., A. Adcroft, C. Hill, L. Perelman, and C. Heisey (1997b), A finite volume, incompressible Navier-Stokes model for studies of the ocean on parallel computers, *J. Geophys. Res.*, 102(C3), 5753–5766, doi:10.1029/96JC02775.
- Mellor, G. L. (Ed.) (2004), *Users Guide for a Three-Dimensional, Primitive Equation, Numerical Ocean Model*, 56 pp., Princeton Univ. Press, Princeton, N. J.
- Mellor, G. L., and T. Yamada (1982), Development of a turbulence closure model for geophysical fluid problem, *Rev. Geophys. Space Phys.*, 20, 851–875.
- Michallet, H., and G. N. Ivey (1999), Experiments on mixing due to internal solitary waves breaking on uniform slopes, *J. Geophys. Res.*, 104(C6), 13,467–13,477, doi:10.1029/1999JC900037.
- Namin, M., B. Lin, and R. Falconer (2001), An implicit numerical algorithm for solving nonhydrostatic free surface flow problems, *Int. J. Numer. Methods Fluids*, 35, 341–356.
- Pietrzak, J., J. B. Jakobson, H. Burchard, H. J. Vested, and O. Petersen (2002), A three-dimensional hydrostatic model for coastal and ocean modelling using a generalised topography following coordinate system, *Ocean Modell.*, 4(2), 173–205.
- Roe, P. L. (1985), Some contributions to the modelling of discontinuous flows, in *Large-Scale Computations in Fluid Mechanics*, edited by B. E.

- Engquist, S. Osher, and R. C. J. Somerville, *Lect. Appl. Math.*, 22, 163–193.
- Saad, Y. (2000), *Iterative Method for Sparse Linear Systems*, 2nd ed., SIAM, Philadelphia, Pa.
- Scotti, A., R. C. Beardsley, and B. Butman (2007), Generation and propagation of nonlinear internal waves in Massachusetts Bay, *J. Geophys. Res.*, 112, C10001, doi:10.1029/2007JC004313.
- Smagorinsky, J. (1963), General circulation experiments with the primitive equations: I. The basic experiment, *Mon. Weather Rev.*, 91, 99–164.
- Stansby, P., and J. Zhou (1998), Shallow-water flow solver with nonhydrostatic pressure: 2-D vertical plane problem, *Int. J. Numer. Methods Fluids*, 28, 541–563.
- Stelling, G. S., and M. Zijlema (2003), An accurate and efficient finite difference algorithm for nonhydrostatic free surface flow with application to wave propagation, *Int. J. Numer. Methods Fluids*, 43(1), 1–23.
- Turner, J. S. (1973), *Buoyancy Effects in Fluids*, 367 pp., Cambridge Univ. Press, Cambridge.
- Vlasenko, V., and K. Hutter (2002), Numerical experiments on the breaking of solitary internal waves over a slope-shelf topography, *J. Phys. Oceanogr.*, 32(6), 1779–1793.
- Woo, S. B., and P. L. F. Liu (2001), A Petrov-Galerkin finite element model for one-dimensional fully nonlinear and weakly dispersive wave propagation, *Int. J. Numer. Methods Fluids*, 37, 541–575.
- Yuan, H., and C. H. Wu (2004), A two-dimensional vertical nonhydrostatic σ model with an implicit method for free surface flows, *Int. J. Numer. Methods Fluids*, 44, 811–835.
- Zhou, J. G., and P. K. Stansby (1999), An arbitrary Lagrangian-Eulerian (ALE) model with nonhydrostatic pressure for shallow water flows, *Comput. Methods Appl. Mech. Eng.*, 178, 199–214.
- Zijlema, M., and G. S. Stelling (2005), Further experiences with computing nonhydrostatic free surface flows involving water waves, *Int. J. Numer. Methods Fluids*, 48(2), 169–197.

R. C. Beardsley, Department of Physical Oceanography, Woods Hole Oceanographic Institution, Woods Hole, MA 02543, USA.

C. Chen, G. W. Cowles, and Z. Lai, School for Marine Science and Technology, University of Massachusetts-Dartmouth, New Bedford, MA 02744, USA. (z.lai@umassd.edu)